A Combined Experimental and Theoretical Study of the Optical Behavior of Se-Ge-Ga-Sb Chalcogenide Thin Films.

A.M. Shakra*[1], R. A. Mohamed[1], Mahmoud Y. El-Bakry[1], Rokia Mahmoud Ali[1], D. M. Habashy[1].

1. Department of Physics, Faculty of Education, Ain Shams University, Roxy, Cairo 11757, Egypt.

This study focused on the characterization of optical properties for chalcogenide glass ($Se_{49.94}Ge_{31.38}Ga_{7.38}Sb_{11.30}$) prepared via quenching procedure and was thermally deposited on glass substrates by thermal evaporation process. The amorphous nature of the evaporated films was confirmed through X-ray diffraction analysis. The composition of the prepared sample was obtained using energy dispersive X-spectroscopy (EDX). The optical properties of the thin films, including transmittance (T), reflection (R), thickness (t), and index of refraction (n), were investigated using spectrophotometry (190-2500 nm). The Swanepoel technique was employed to calculate the thickness and n values from the transmission data. Wemple-DiDomenico (WDD) model used to estimate dispersion factors (E_o and E_d) and dielectric constants from the refractive index data. The optical energy gap (E_g^{opt}) for the studied composition was determined. The optical absorption analysis revealed both permitted direct and indirect transitions. To model the optical constants, an artificial neural network (ANN) was trained using experimental data. Various ANN configurations were tested, and the best one with minimal error was selected. The ANN model demonstrated a satisfactory match with the findings. A mathematical equation describing the optical behavior of the samples was derived. The selected ANN model's performance was admirable, as it could accurately predict optical parameters for unmeasured thicknesses. In conclusion, the ANN approach proved to be a valuable tool for modeling the optical properties of $Se_{49.94}Ge_{31.38}Ga_{7.38}Sb_{11.30}$ thin films, exhibiting high accuracy and excellent predictive capability.

Keywords

Optical properties; Chalcogenide glasses; Modeling; Prediction; and Artificial Neural Network ANN model .

* amshakra@yahoo.com, amerahsanen@edu.asu.edu.eg, doaamahmoud@edu.asu.edu.eg

Receive Date: 4-7-2024; Revise Date: 20-7-2024; Accept Date: 22-7-2024; Publish online : 23-07-2024

Introduction

Chalcogenides (ChGs) have great attention in research due to its important applications [1], commercial importance, electronics applications in devices, particularly, in the area of thin films [2-4]. Chalcogenide glasses (ChGs.) contains one or more chalcogen [Sulphur (S),Selenium (Se) or Tellurium (Te)] [5], [6]. They are important due to high transparency, restricted optical absorption, reversible transformation of phase, large refractive index, etc. [7, 8].

The optical properties of Chalcogenide glasses, such as their refractive index and transmittance in the infrared spectrum, explain why filters, antireflection coatings, and other optical devices are interested in using them. [9-11]. Chalcogenide glasses can have their thermal, optical, electrical and mechanical properties changed by adding impurities, producing new and improved materials for the device industry. The nonlinear characteristics of chalcogenides, which favored for nonlinear optics, are much higher than ordinary glasses [12]. Hence, chalcogenides are recently used for producing military and medical applications [13,14]. By altering the doping components and substrate film deposition techniques, ChGs. can have different properties [15]. Several authors [16-19] studied the optical response for different materials.

Selenium and tellurium are widely used in amorphous ChGs., [20]. Because of their broad transparency window, good thermal stability [21], high ability of forming glass [20], and attractive and commercial applications [22], Se-based materials are preferred [20, 22]. The disadvantages of pure selenium can be summed up as low sensitivity and short lifetime [23] and great unitability, which restrict ChGs. applications. But by combining Se with elements like Sb, Ga, and Ge, that can be avoided [23]. These impurities increase the electrical conductivity, thermal stability, and photosensitivity of the pure Se-material [22].

Ge-Sb-Se ternary glasses are important materials for infrared optical fiber applications because of their good mechanical, chemical, and thermal properties. Many properties of Ge-Sb-Se glasses are attractive for researchers [24, 25]. Ga doping glasses turn out to be the best materials for creating lasers, amplifiers, doping sources, and other photonic devices in the mid-IR range [22, 26]. The application of Ge-Sb-Ga thin films in phase-change memory and other non-volatile memory devices has been extensively studied. These films have phase transitions states, making them suitable for data storage applications .Research has also been done on the thermoelectric properties of Ge-Sb-Ga thin films, which are useful in thermoelectric generators and coolers .

In previous studies of Se-Ge-Ga–Sb compound [20, 21], the addition of the fourth element Sb, which is a member of group V, results in a quaternary composition that enhances stability [27], and glass-ability while also causing compositional disorder.

Additionally, Sb improves the optical characteristics of Se-Ge-Ga by lowering the optical bandgap energy [20]. Germanium as a matrix increases the glass formation area. The Se-Ge-Ga-Sb alloy became appealing for use in storage applications and is now being considered as a possible mid-IR fiber material [28]. There are many technological applications of thin film in infrared oscillations, light emitting diodes, lasers, infrared detectors, etc.[29-31]. In addition to their good chemical and physical features,which can be used in high-precision molding technology [32]. These properties make this type of material highly recommended for mid- and far-infrared applications [33] such as IR (infrared) lenses and IR detectors and suitable for producing different medical, military,and civil applications [34].

It is found that while binary and ternary glasses have received a lot of attention in the literature, quaternary glasses, which may have even greater applications, have received less research and study. Recently, many researchers have studied different quaternary chalcogenides [35-39]. Hence, Se-Ge-Ga-Sb quaternary compound was chosen for our work due to its industrial applications and we investigated the optical behavior of Ga–Sb–Ge–Se films then were compared with the training and prediction outcomes.

In the current research, the optical behavior of the evaporated $Se_{49.94}Ge_{31.38}Ga_{7.38}Sb_{11.30}$ thin film composition is described, by using transmission spectrum at wavelength range190–2500 nm. Also, the optical constants are presupposed and investigated. Along with dielectric constants, the Wemple and Di-Domenico Parameters and the connection between the measured parameters [40, 41] are also examined. Our findings were consistent with earlier research on chalcogenide glass [42, 43]. Using Tauc's extrapolation method, the non-direct transition model is utilized in the computation of the optical band gap for the studied composition [44]. The acquired values provided a clear understanding of the optical behavior of the amorphous investigated composition [45].

ANN model gains many advantages, storing information on the entire network instead of storing it on the database. That enables the network to train despite the presence of a few missing pieces of experimental data. The parallel processing capability provides the ANN network with the strength to carry out multiple tasks concurrently. The most important advantage of ANN is the ability to make machine learning and make decisions by generating results for similar events. Lately, there has been a lot of focus on using ANN in modeling many physical properties. ANNs Developments and applications have been used in modeling many relations in physics [46-58]. Additionally, ANN based on the algorithm known as resilient backpropagation, or R-prop are utilized to calculate the optical parameters of the understudied semiconductor. The resilient back-propagation algorithm (Rprop) is considered one of the fastest methods for training artificial neural networks R-prop is a gradient-free

optimization algorithm, meaning it does not rely on gradient information directly. Instead, it adjusts learning rates for each weight based on the direction of the weight updates from one iteration to the next. By adapting learning rates dynamically and independently for each weight, R-prop can potentially converge faster and more reliably compared to traditional methods. It is particularly useful in scenarios where gradient information might be noisy or unreliable (such as with sigmoid activations). In summary, R-prop enhances the efficiency of ANN training by mitigating issues related to the partial derivatives from sigmoid functions and by dynamically adjusting learning rates based on the direction of weight updates. This makes it a valuable alternative to traditional back-propagation algorithms, especially in scenarios where sigmoid activations are prevalent.

The ANN network accepts the experimental data as inputs. The training is processed many times to obtain the minimum error. The ANN modeling process is performed to simulate the transmittance T(λ), the reflectance R(λ), the refractive index $n(\lambda)$, the absorption index $k(\lambda)$, and dielectric constant ε_1 of different thicknesses of $Se_{49.94}Ge_{31.38}Ga_{7.38}Sb_{11.30}$ thin films.A mathematical equation representing the optical behavior of the mentioned semiconductor is obtained. Also, Prediction of T(λ), R(λ), $n(\lambda)$, $k(\lambda)$, and ε_1 for values that are not included in the trained datasets. This work aims to study the effect of film thicknesses variation of $Se_{49.94}Ge_{31.38}Ga_{7.38}Sb_{11.30}$ on the optical properties and using ANN model in obtaining the optical constants of investigated thin films. The corresponding experimental findings were compared with the training and prediction outcomes.

1. Experimental

1.1. Materials

Sample in bulk form of $Se_{49.94}Ge_{31.38}Ga_{7.38}Sb_{11.30}$was made using the melt-quenching method in several steps. First, each component was weighed using electronic balance in accordance with their stoichiometric ratio (total weight: 5 gm). Next, they were poured into an empty silica ampoule that had been cleaned before and sealed under a vacuum of 1.332×10^{-6} kPa. The tube was then placed in a swing oven. Melting point (MP) Ga was set at 30 ^{o}C, and the oven temperature was increased to 50 ^{o}C. The temperature was then raised gradually with rate 50 ^{o}C/h to the melting point (MP) of selenium at 220 ^{o}C and maintained there for two hours. After that, the temperature was raised slowly to the MP of Sb at 640 ^{o}C and maintained there for an additional two hours. Finally, the temperature was raised to 950^{o}C (MP of Ge ≈ 940^{o}C) and remained constant for 20 hours. (The homogeneity of the compound was achieved by long time of preparation and mechanical oscillations of the mixture in vibration oven).

The studied sample was then got in amorphous state by quenching the molten sample in the ampoule with ice water. The finely separated powder was made by crushing the

evaporation-related tube ingot. With the aid of thermal evaporation technology and a high vacuum coating device (model Edwards E306 A), thin films of the prepared mixture were produced on a glass substrate that had already been cleaned with a deposition rate of 5 nm. /s. To create uniform layered films on a flat surface, the substrates were fastened to a suitably rotatable holder. The substrates were fixed onto arotatable holder (up to 240 rpm) to obtain homogeneous deposited films at adistance of 25 cm above the evaporator. Room temperature was maintained as the substrate's temperature during deposition procedure.

2.2 Measurments

EDX (Energy dispersive X-ray) detector and a scanning microscope (Jeol JSM 5400, Tokyo, Japan), the composition of the films as they were deposited at a 30 kV acceleration voltage was investigated. The analyzed samples are also examined using a Philips X-ray diffractometer equipped with a copper target. The samples under investigation were subjected to (XRD) using a Ni filter operating at 40 kV and 20 mA. X-ray diffraction patterns in the 4^{o} to 90^{o} angular range, measured at room temperature. A calibrated double beam spectrophotometer measured the transmission and reflection for the studied films at normal incidence using unpolarized light at room temperature in λ range of 190–2500 nm, (Tokyo, Japan).

One method for machine learning is the artificial neural network (ANN) model. A processing element of an ANN model is a neuron Fig. (1). A neural network architecture has multiple layers (input, hidden layers, and output) involving multiple nodes (neurons). Hidden layers are the layers where the nodes are organized. Weights are the ties that bind them to one another. In principle, training is regarded as the primary ANN operating phase. The training process involves adjusting the weights (w) and biases (b) until the performance becomes acceptable. The resilient back-propagation algorithm (R-prop) is considered a fast method for ANN training. The importance of the (R-prop) algorithm is to remove the negative effects of partial derivatives applied to the output that are caused by log-sig transfer functions (sigmoid functions).

The partial- derivative is the ratio between the yield derivatives to the weights. The derivative sign is the factor used to obtain the course of the following weight adjusting process while the derivative size is not significant in the process. An independent update value is utilized to obtain the amount of change. However, the algorithm changes the updated value by comparing the sign of the weight with its sign in the last epoch. If the sign does not change during several iterations the updated value increases and vice versa. That prevents weight oscillations and directs them to error minimization. [59], [60]

Training the ANN network includes certain steps. The first step is processed by identifying the input and target parameters. The second step includes the selection of the best ANN structure based on the validation of ANN performance.

Finally, forecast values that weren't used during system training. A learning algorithm is defined as a procedure for altering a network's weights (w) and biases (b) to reduce the error between the targets and the ANN outputs. The mean squared error (MSE) was calculated using Eq. (1):

$$MSE = \frac{1}{n}\sum_{i=1}^{n}(e_i)^2 \qquad (1)$$

Where *n* is inputs and e_i is the produced errors.

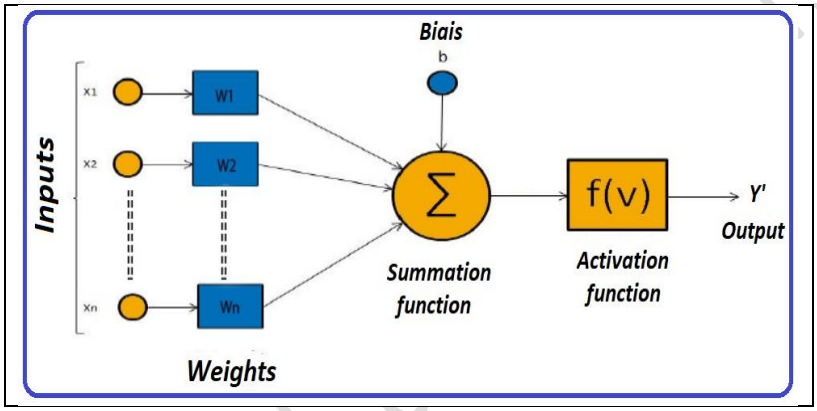

Fig.(1) Schematic diagram of an artificial neuron.

A multilayer neural network (ANN) that uses the back- propagation (BP) learning algorithm is the most well-known type of ANN. The computation of BP is the best of the multi-layer computations. A multilayer feedforward ANN structure is a mixture of different layers Fig.(2). The First tier is a data tier that represents the training data, which is thereafter ready and transmitted to the last tier (output tier) through at hidden tiers (HT). Neurons required in each hidden tier are important in network design. The best number. of neurons and HT depend on factors such as the inputs, the targets, the data noise, the error function, the design of the network, and the trained algorithm.

Training a network involves continuously processing input patterns and adjusting the connection weights between the necessary output components related to the network. Fig. (3) represents the block schematic of the backpropagation network. The purpose of training is to decrease errors that represent the subtraction between the targets and the ANN results, to achieve the best performance. Thus, MSE should be minimized [61,62].

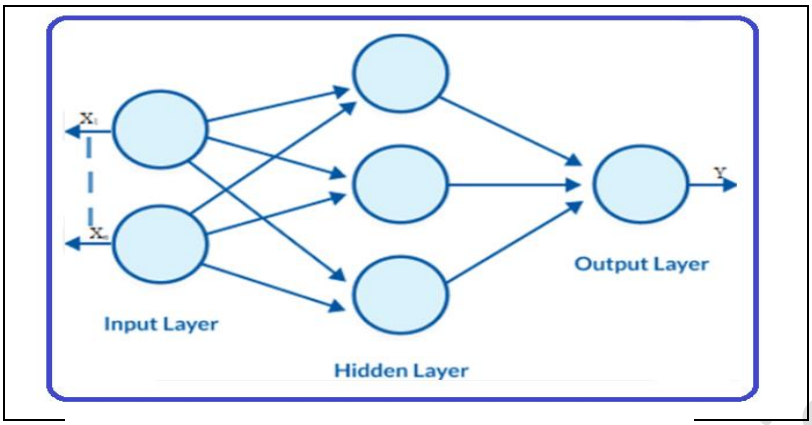

Fig.(2) ANN Representative architecture .

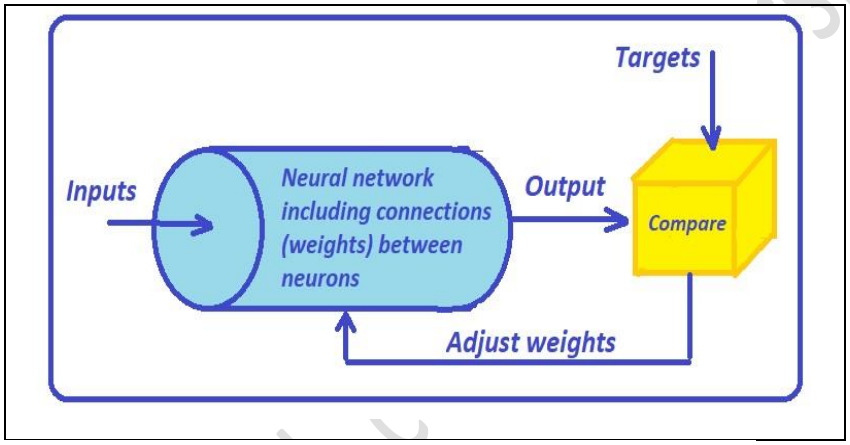

Fig.(3) The flow of BP learning algorithm.

During training, inputs contain three parts: (70%) training set, (15%) test set, and (15%) validation set. This classification's goal is to make sure that the ANN model is validated by contrasting its targets with the random value predictions. The Levenberg-Marquardt algorithm is presented in Eqs. (2 – 6). The error function is summing squared errors.

$$f = \sum_{i=1}^{n} e_i^2 \qquad (2)$$

Where n is the inputs. The Jacobian matrix of the error is defined as

$$J_{ij} = \frac{\partial e_i}{\partial w_j} \qquad (3)$$

For $i = 1, \dots, n$ and $j = 1, \dots, m$

Where the Jacobian matrix size is $n.m$.

The error gradient is presented in Eq. (4)

$$\nabla f = 2\boldsymbol{J}^T.\boldsymbol{e} \qquad (4)$$

Where $\boldsymbol{e}$ is the error vector. Then, the approximated matrix is defined in Eq. (5)

$$\boldsymbol{H}f \approx 2\boldsymbol{J}^T.\boldsymbol{J} + \lambda \boldsymbol{I} \qquad (5)$$

Where λ is the damping and I is the identity matrix. The Levenberg – Marquardt parameters are computed using Eq. (6)

$$w^{(i+1)} = w^{i} - \left(\boldsymbol{J}^{(i)T}.\boldsymbol{J}^{(i)} + \lambda^{(i)}\mathbf{I}\right)^{-1}.\left(2\boldsymbol{J}^{(i)T}.\boldsymbol{e}^{(i)}\right) \qquad (6)$$

The Levenberg-Marquardt algorithm is a hybrid algorithm that merges the benefits of Newton's method and gradient descent. It works by adjusting a damping parameter λ between two extremes: zero and a large value. When λ is zero, the algorithm converts to Newton's method which is a fast but unstable algorithm. When λ is large, it converts to gradient descent which is a stable algorithm. The algorithm starts by initializing λ to a large value. This leads to slow conversion to gradient descent. This process of adjusting λ typically accelerates the convergence to the minimum. [63].

The MSE and R are computed using Eys. (7) and (8) [63].

$$\mathrm{MSE} = \sum_{t=1}^{n} (\mathrm{O_i} - \mathrm{T_i})^2 / \mathrm{n} \qquad (7)$$

$$R = \sqrt{1 - \left(\frac{\sum_i (\mathrm{O_i} - \mathrm{T_i})^2}{\sum_i (\mathrm{O_i})^2}\right)} \qquad (8)$$

where n denotes the data points, $\mathrm{T_i}$ is the model's output, and $\mathrm{O_i}$ denotes the experimental goal.

3. Results

Structure of $Se_{48.62}Ge_{28.09}Ga_{6.34}Sb_{11.30}$ Thin Films

EDX analysis revealed the composition and homogeneity of the investigated samples, indicating that the respective atomic percentages of Se, Ge, Ga, and Sb are 49.94 %, 31.38%, 7.38% and 11.30%, respectively, as depicted in Fig.(4a). Fig. (4b) shows the morphology of the outer layer of the sample ($Se_{49.94}Ge_{31.38}Ga_{7.38}Sb_{11.30}$) from the scanning microscope. The formulation of this specimen ($Se_{49.94}Ge_{31.38}Ga_{7.38}Sb_{11.30}$) indicates a close resemblance in elemental proportions to those found in the laboratory-made ingot as shown in table1. Furthermore, the analysis confirmed the absence of any unusual components in the sample under investigation.

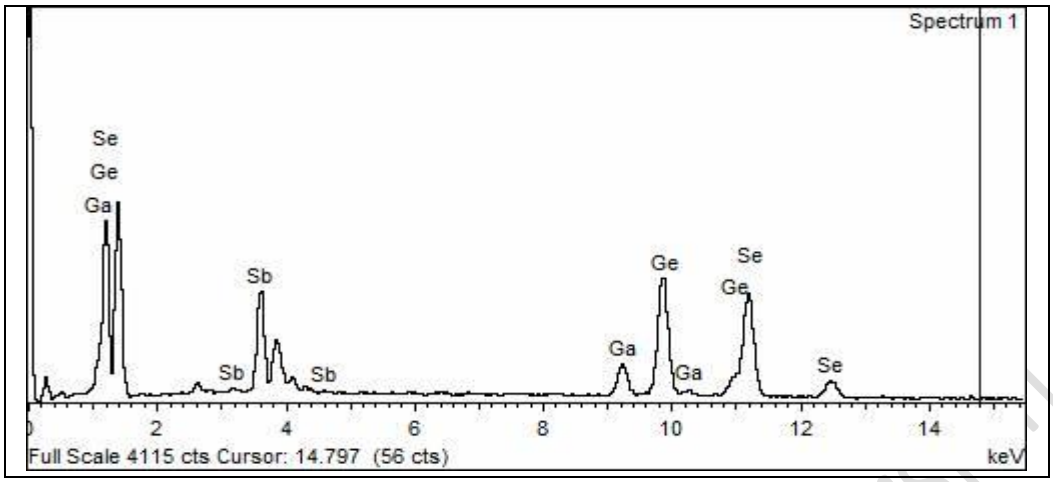

Fig. (4a) EDX spectra and surface morphology of the thin film sample $Se_{49.94}Ge_{31.38}Ga_{7.38}Sb_{11.30}$.

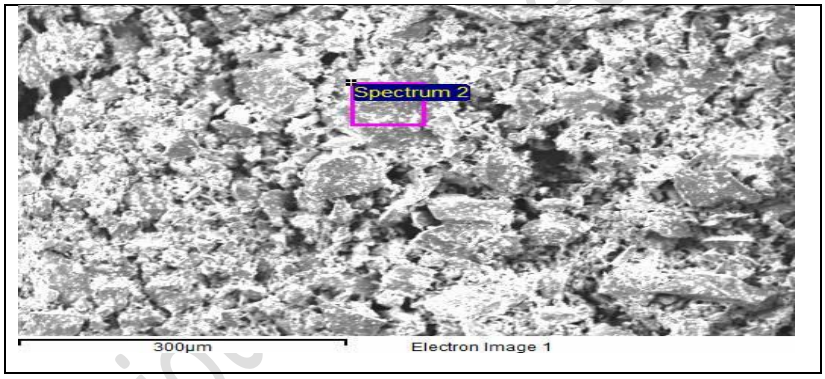

Fig. (4b) shows the morphology of the outer layer of the sample ($Se_{49.94}Ge_{31.38}Ga_{7.38}Sb_{11.30}$ $at\%$) from the scanning microscope.

Table 1. The EDX data for $Se_{49.94}Ge_{31.38}Ga_{7.38}Sb_{11.30}$ Thin film.

The actual formula	Se (at. %)	Ge (at. %)	Ga (at. %)	Sb (at. %)
$Se_{49.94}Ge_{31.38}Ga_{7.38}Sb_{11.30}$	49.94	31.38	7.38	11.30

XRD for the evaporated $Se_{49.94}Ge_{31.38}Ga_{7.38}Sb_{11.30}$Thin-film sample is shown as an example in Fig. (5). This pattern exhibits an amorphous phase upon analysis. On the composition chart, there is a wide hump and no peaks can be seen. This happens due to the molecules that evaporated haphazardly on the substrate. There is an agreement between the obtained result of X-ray analysis with other studies [64,65]

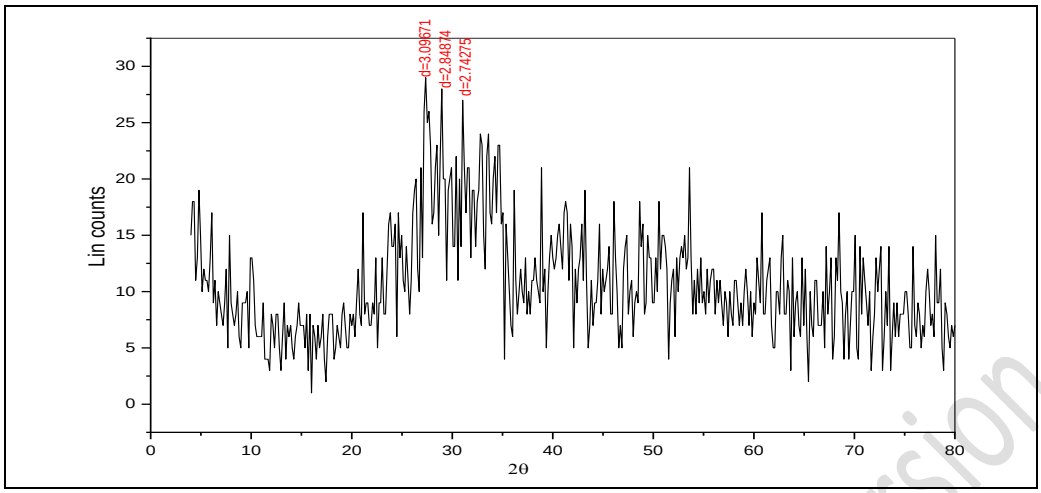

Fig. (5). XRD pattern for $Se_{49.94}Ge_{31.38}Ga_{7.38}Sb_{11.30}$thin-film sample as example.

Optical Properties of $Se_{49.94}Ge_{31.38}Ga_{7.38}Sb_{11.30}$thin- films.

Understanding the specimen's electronic nature requires knowledge of the optical absorption of the composition under examination, particularly the absorption edge [66, 67]. The optical parameters were ascertained using the spectral distribution of transmission using Swanepoel's method [67].

The Spectral Distribution of the Films Under Study's T(λ) and R(λ).

Regarding the films that were examined at various thicknesses, the variations in T(λ) and R(λ) with wavelength were obtained at normal incidence with a range of λ (190-2500 nm) at (303 K), see Fig.(6a, b). As seen in these images, at high λ (1900-2500 nm), T + R =1, indicating the film transparency without any absorption or scattering taking place; extinction coefficient k ≈ 0 [73, 74]. The T and R along (λ nm) for $Se_{49.94}Ge_{31.38}Ga_{7.38}Sb_{11.30}$for all studied films in Fig. (7). The reflection spectrum's minimum occurs at roughly the same λ as the transmission spectrum's maximum and vice versa. This demonstrates the optical homogeneity of the deposited layers [66, 70].

Fig (6a) shows comparative transmittance spectra for films of different thicknesses. As observed, there is a redshift with increasing film thickness in interference-free region,

accompanied by changes in the position of fringes at low energy. This redshift in T(λ) indicates that light form (holes) in films below the absorption edge in the Urbach tail [71].

The Swanepoel approach [67], which solely considers significant fringes of interference in the T(λ) spectrum used to assess the optical characteristics of the films.

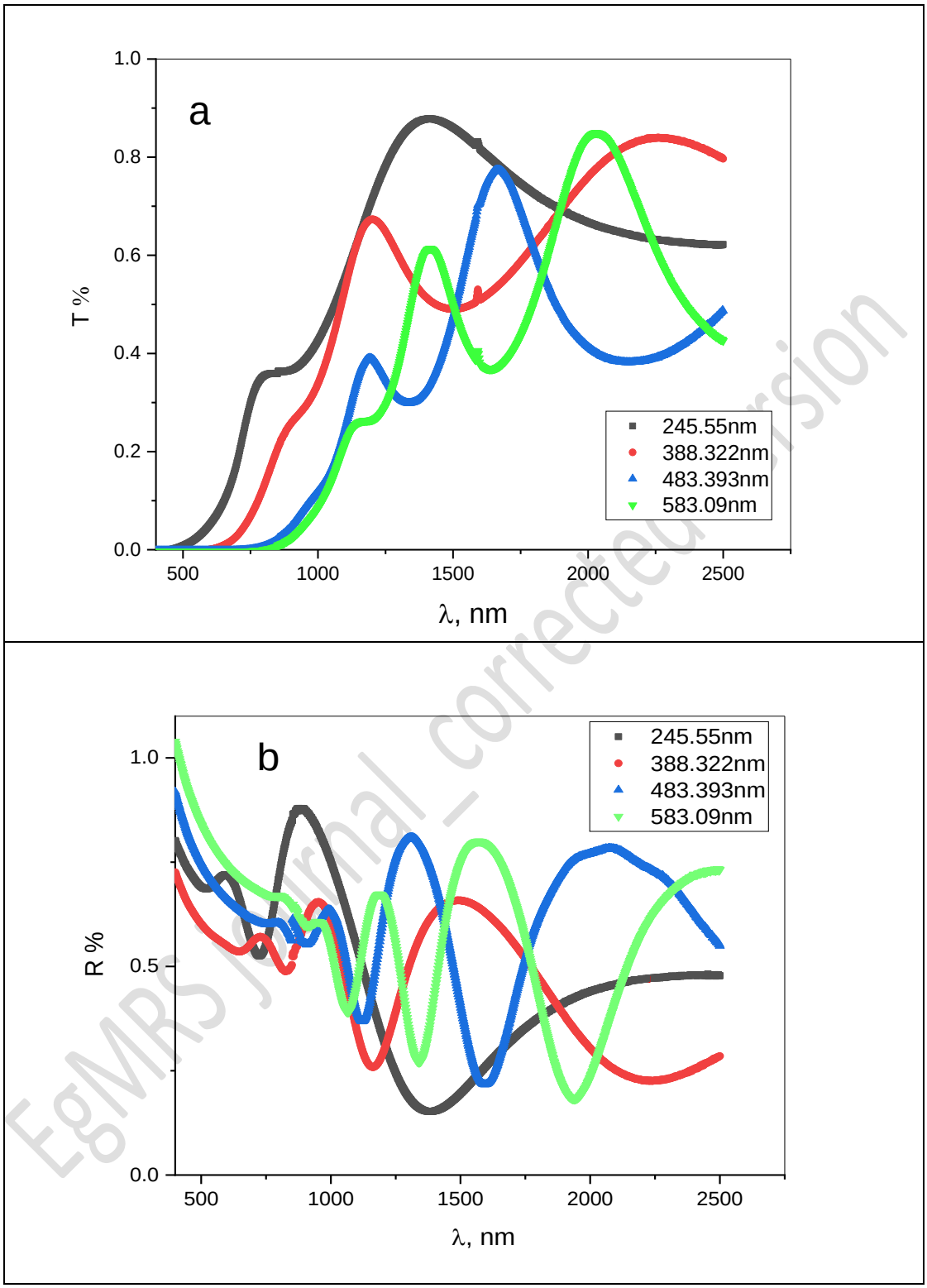

Fig.(6a&b). Distribution of spectra of (T) and (R) for $Se_{49.94}Ge_{31.38}Ga_{7.38}Sb_{11.30}$Films.

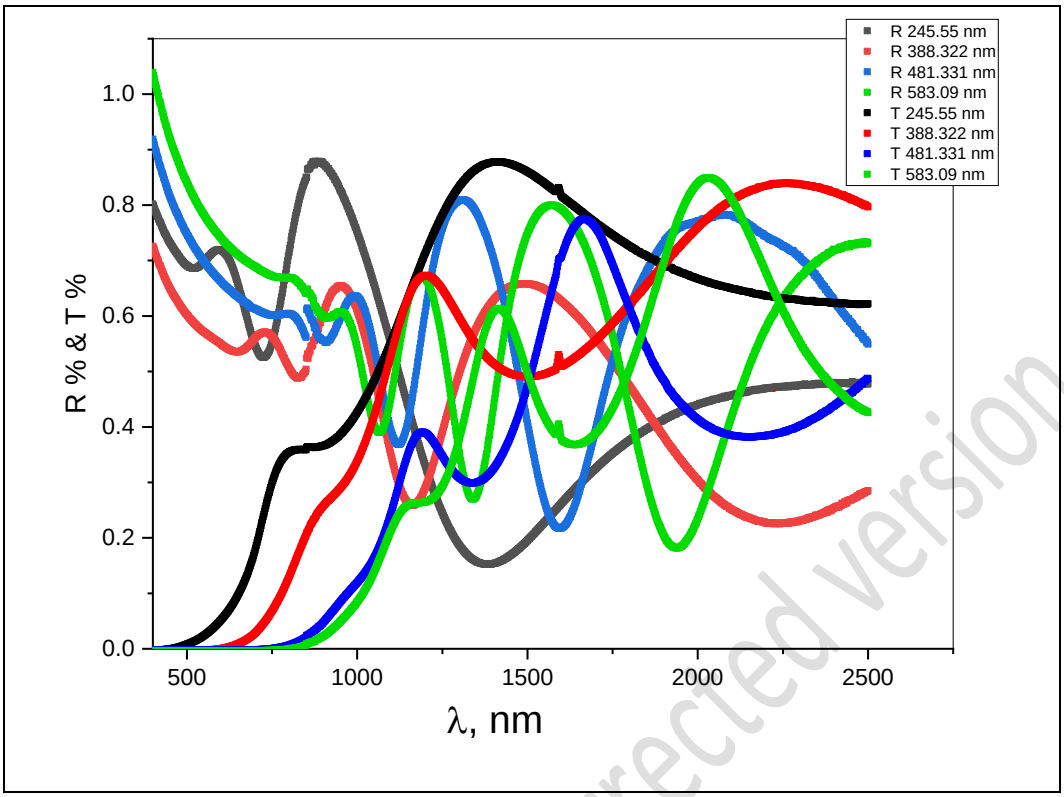

Fig.(7). T (λ) and R(λ) spectra of $Se_{49.94}Ge_{31.38}Ga_{7.38}Sb_{11.30}$films.

Refractive index (n) and film thickness estimation.

Using Manifacier et al.'s concept [70], Swanepoel's method [67] can be used to get the thickness (t) and the refractive index (n) for the films from T(λ) spectrum. This method depends on the creation of T_m and T_M envelopes between minimum and Maximum of the T(λ) spectrum. Finding the initial refractive index n_i is made possible by utilizing formula [67] knowing the envelopes and the tangent points of T(λ) spectrum:

$$n_i = \sqrt{[M + (M^2 - S^2)^{1/2}]} \qquad (9)$$

Where,

$$M = 2S\,\frac{T_M - T_m}{T_M T_m} + \frac{s^2+1}{2} \qquad (10)$$

and S = 1.5 is the glass's refraction index. The values T_m and T_M represent the envelope lines' tangent points at particular wavelengths.

To get a rough estimate of the film thickness, use formula [67]:

$$t_i = \frac{\lambda_1 \lambda_2}{2(\lambda_1 n_2 - \lambda_2 n_1)} \quad (11)$$

Where n_1 and n_2 are refractive indices at λ_1 and λ_2 , that are maxima (or minima). The initial thickness values $\overline{t_i}$ were then computed. These variables are required by the equation of interference fringes $2n_i\overline{t_i} = m_o\lambda$ to obtain m_o, or "the order number of extremes," along with n_i. The exact value of $\overline{t_i}$ is then greatly increased by using the integer or half-integer of m_o and converting it to a value for m_f. As a result, there is less variance, and the final thickness $\overline{t_f}$ can be calculated.

n can then evaluate using the average of ($\overline{t_f}$) and the accurate value of m_f using $2n\overline{t_f} = m_f\,\lambda$. It is possible to fit *n* for the films using Cauchy equation [68]. A formula that

employed in the extrapolation at small (λ) is $n = a + b/\lambda^2$, as the inset of Fig.(8) illustrates.

Asummary of ***a*** and ***b*** values over the range of λ is given in Table 2. For varying thicknesses, the measured refractive index *n* of the films that were deposited shows a spectrum variation consistent with the estimated values of the Cauchy relation (See Fig. 8).

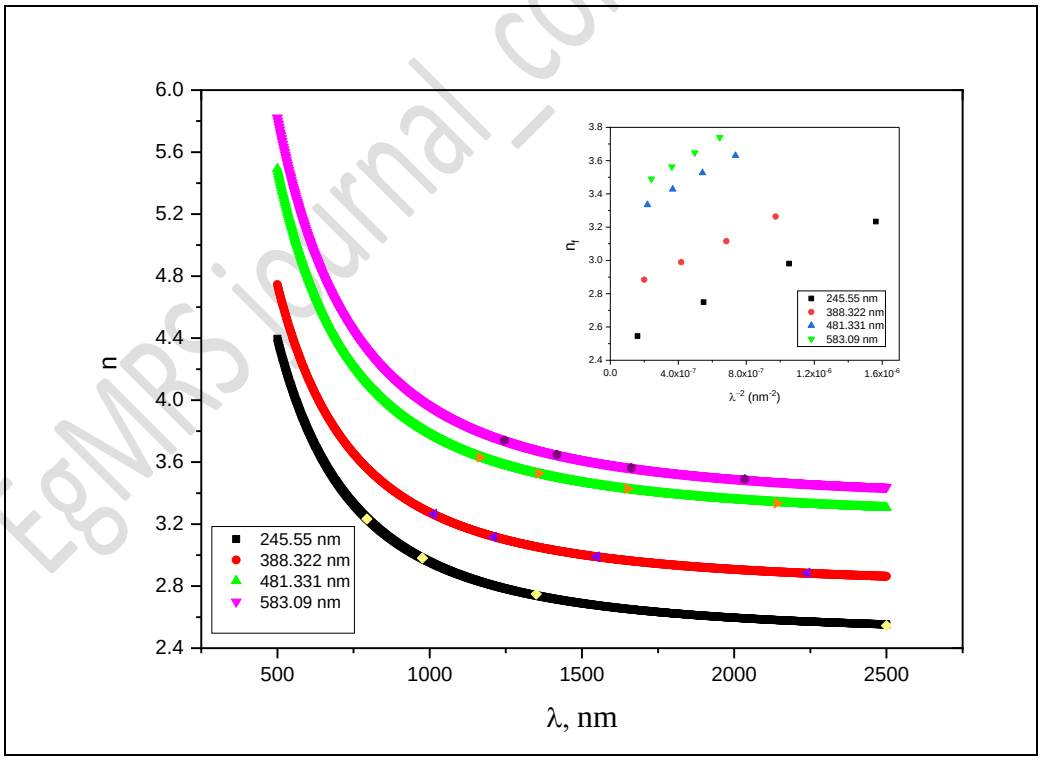

Fig. (8). The films under investigation's refractive index spectral distribution. Inset: The as-deposited films' Cauchy equation fit.

Table 2 a and b parameters according to Cauchy for $Se_{49.94}Ge_{31.38}Ga_{7.38}Sb_{11.30}$ films.

Thickness, (t_f)	a	b
245.55 nm	2.48	479747
388.32 nm	2.79	489883
481.33 nm	3.22	569154
583.09 nm	3.34	620704

In the spectral range where absorption is prominent (< 670 nm), as depicted in Fig. (8), the refractive index (n) shows higher values at shorter wavelengths. As the wavelength increases, the refractive index gradually decreases and stabilizes above 1500 nm.

Extinction coefficient k and Absorption Coefficient α estimation.

Given (n) and (t) values, we calculate (α) using Swanepoel equation [67] to estimate *x* (the absorbance) in the region of fundamental edge.

$$\alpha = \frac{1}{t} ln(x^{-1}) \qquad (12)$$

i. When strong absorption region exists, where the minimum and maximum interference merge into a single line T_o, *x* is obtained by the formula:

$$x = \frac{(n+1)^3(n+s^2)}{16n^2s} T_o \qquad (13)$$

ii. For a region of weak and moderate absorption, the absorption *x* is evaluated from the extreme interference values using the equation:

$$x = \frac{E_M - [E_M^2 - (n^2-1)^3(n^2-s^4)]^{\frac{1}{2}}}{(n-1)^3(n-s^2)} \qquad (14)$$

where $E_M = \frac{8n^2s}{T_M} + (n^2-1)(n^2-s^2)$

The coefficient k was calculated, knowing the value of α at λ.

$$k = \frac{\alpha\lambda}{4\pi} \qquad (15)$$

k and λ relation shown in the Fig. (9).

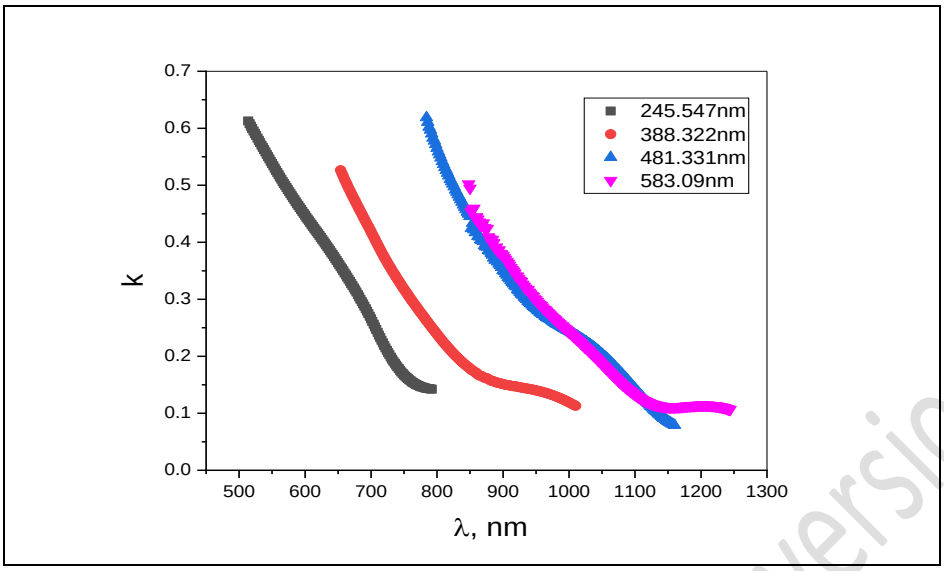

Fig.(9). k coefficient with λ for films under study.

Obtaining the energy gap E_g^{opt} and evaluating α.

The optical absorption research [12] provides a clear explanation for a few bands structure and energy gaps of materials. The edge of absorption for various amorphous materials can be split into two regions of absorption according to the energy (low and high) of α as calculated by the Swanepoel method [68, 69]. Fig. (10) illustrates how the films under investigation's α varies with photon energy ($h\nu$).

The edge that absorbs energy is split into two parts based on (α) values:

The absorption at low $h\nu$ generally follows Urbach's rule in the first region, which is for low values of $\alpha < 10^4$ cm^{-1} [73]. As shown from eq. (16), absorption of this part is caused by transitions in localized states in one band's exponential tail and the other band extended states:

$$\alpha(h\nu) = \alpha_{\circ} exp(h\nu/E_e) \qquad (16)$$

$\alpha_{\circ}$ (constant), E_e (Urbach's energy), which, for amorphous semiconductors is the disorder degree and is defined by the width of localized states tail in optical energy gap [74, 75]. Fig. (10) shows log α versus $h\nu$. Equation (16) allows the deduction of the E_e and $\alpha_{\circ}$ values, as seen in table 3 and result from the least-square fitting of the first region.

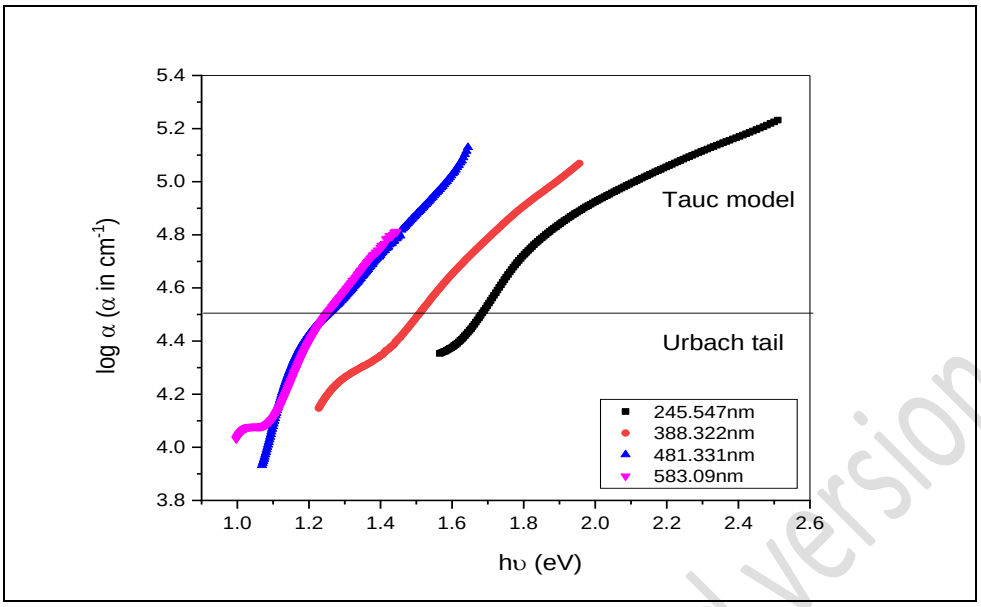

Fig.(10). log(α) versus Photon energy $h\nu$.

Table 3. E_e, α_o. E_g^{dir}, E_g^{ind}values for $Se_{49.94}Ge_{31.38}Ga_{7.38}Sb_{11.30}$ films.

Thickness t (nm)	E_e (eV)	α_o $(cm)^{-1}$	E_g^{dir} (eV)	E_g^{ind} (eV)
245.547 nm	0.26	44.70	1.68	1.28
388.322 nm	0.26	98.80	1.58	1.22
481.331 nm	0.27	291.05	1.39	1.08
583.09 nm	0.2720	324.5047	1.38	1.05

According to Tauc's law [76, 77], the second part corresponds to greater absorption coefficients $\alpha \geq 10^4$ cm^{-1} and is connected to transitions in conduction and valence bands. following the formula:

$$\alpha h\nu = A(h\nu - E_g^{opt})^r \qquad (17)$$

E_g^{opt}(optical energy gap), edge-width parameter A (The Tauc parameter) represents the film's quality. Tauc parameter can also offer important insights into the disorder that exists in thin films. Increased levels of disorder or defects in structure in the film are indicated by higher Tauc parameter values. It is crucial to remember that the Tauc parameter analysis should be used in combination with other characterization techniques to obtain a thorough understanding of the thin film properties. This information can be used to understand the structural properties, defect states, and overall quality of thin films [78]. A is determined by using the linear part of Eq. (17).

The index parameter (r), which indicates the type of transition, can be theoretically equal to 2, 1/2 for allowed indirect and direct transitions or 3, 3/2 for forbidden ones. The most effective technique to know the type of transition and estimate the related energy value is to plot $(\alpha h\upsilon)^{1/r}$ against $h\upsilon$ using equation (17).

The optical band width is found at the intersection of the photons' energy axis. The ratio $(\alpha h\upsilon)^2$ against $h\upsilon$ yields a line show allowed direct optical transition E_g^{dir} for all studied sample thicknesses, Fig. (12), while Fig. (11) depicts a straight path illustrating the allowed values of indirect optical transitions E_g^{ind} .The photon energy axis (hν) intersected with the linear component to zero absorption at the extrapolation's intersection point to yield the energy gaps E_g^{dir} and E_g^{ind}, which were then entered into the Table 3.

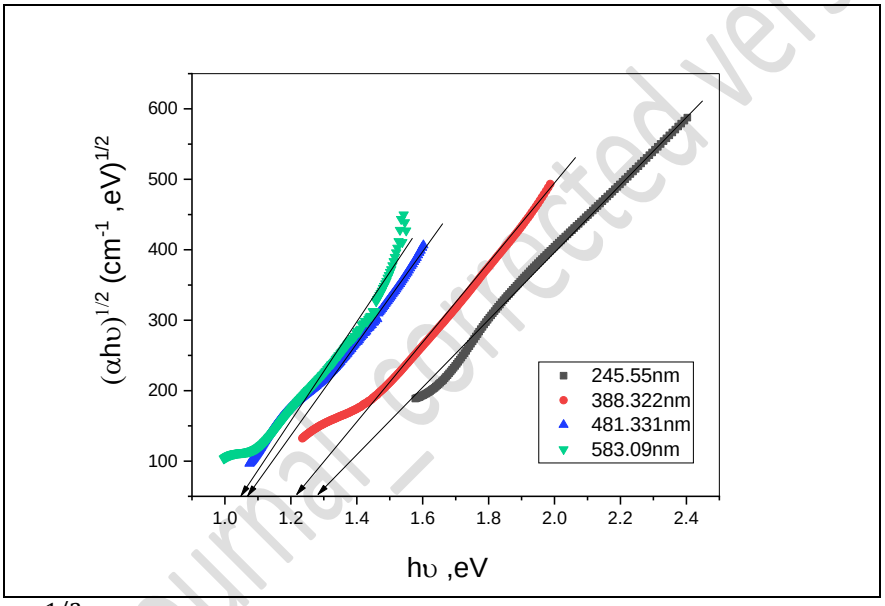

Fig.(11) $(\alpha h\upsilon)^{1/2}$ versus $h\upsilon$ for $Se_{49.94}Ge_{31.38}Ga_{7.38}Sb_{11.30}$ films of different thicknesses.

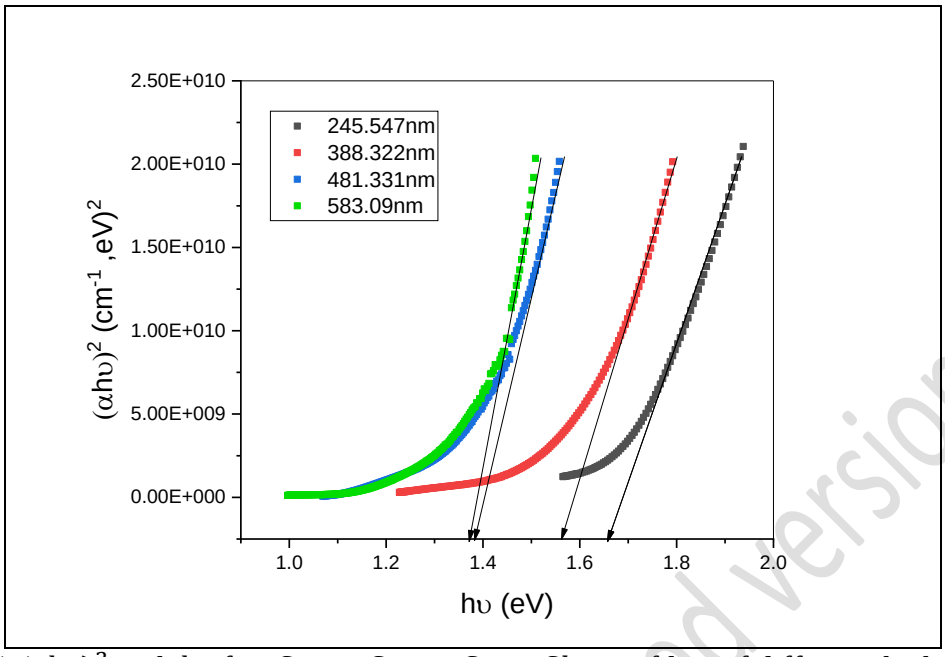

Fig. (12) $(\alpha h\nu)^2$ with hν for $Se_{49.94}Ge_{31.38}Ga_{7.38}Sb_{11.30}$ films of different thicknesses.

Table 3 shows that increasing film thickness associated with changing the predicted energy gap of thin films from 1.68 eV to 1.38 eV for allowed direct transitions and from 1.28 eV to 1.05 eV for allowed indirect transitions. The following interpretation of the thickness's impact on the optical band gap is possible: The transmittance typically drops and switches to higher wavelengths as the thin film thickness grows. This causes the optical absorption edge to shift in the direction of higher wavelengths, which lowers the optical gap energy Sandomirskii [79]. The way that increasing film thickness alters the optical energy gap may be connected to a rise in defects that cause localized states (L.S) to form in the gap and subsequently cause the film band gaps to shrink. In addition, selenium atoms' lone-pair electrons form L.S at the top of V.B tail and the bottom of C.B. These created L.S states cause the forbidden band gap to contract, the tail to broaden, and as a result, the band gap width to decrease [79 -82].

The defects, likely resulting from the existence of structural defects, and decreasing of long-range order generally broaden the edges of amorphous material band. Consequently, the disorder of the system and the band tail width are increased by L.S at or near the edges band [69]. The obtained values of the energy gap in our study are agreement with that reported by Huda Allah Abou-Elnour et all. ($E_g^{dir} = 1.85\ eV$, $E_g^{ind} = 1.2$ eV) [64].

Finding the dielectric constants (ε_L & ε_∞) at high frequency (f).

There are two ways to get dielectric constant ε at high frequency using (n) data [83]. The first approach describes how the lattice vibrational mode of dispersion and free carriers contribute to the real dielectric constant (ε_1). It is well known that, as opposed to the complex refractive index, N=n-ik, the complex dielectric constant has a direct

relationship with the electronic transition in a particular material., $\varepsilon^* = (\varepsilon_1 - i\varepsilon_2)$. How free carriers contribute to (ε_1) could be clarified [66, 69].

$$\varepsilon_1 = n^2 - k^2 = \varepsilon_L - \beta\lambda^2 \qquad (1)$$

where $\beta = \dfrac{e^2 N}{4\pi^2 c^2 \varepsilon_o m^*}$ and $N/m^* = \frac{\varepsilon_o \varepsilon_L}{e^2}\omega_p^2$

where c (velocity of light), ε_0 (dielectric constant for free space), e (charge of electron), ε_L (lattice dielectric constant), N/m^* (ratio of density concentration of free charge carriers to effective mass) . ω_p (plasma frequency) (The resonance frequency for electrons' free variations about their state of equilibrium) and calculated by the ratio:

$$\omega_p^2 = \frac{e^2 N/m^*}{\varepsilon_o \varepsilon_L} \qquad (2)$$

The dielectric constant for free and bound electrons ($\varepsilon_1 = n^2$) is evaluated in non-absorbing (transparent) region (k ≈ 0), with the imaginary part being $\varepsilon_2 = 2nk$. Fig (13) shows the variation of the real part $\varepsilon_1$versus λ^2. Therefore, using Eq. (19) the relation yields a straight line. As film thickness increases, Fig .(13) illustrates that the value of ε_1 rises. A good response of the amorphous films is revealed by these well-obtained results and the effectiveness of dielectric parameters [80]. The values of N / m^* and ε_L were acquired from vertical axis' intersection point and slope, and these results were utilized to get the plasma frequency shown in Table 4. From this table we see that when the film thickness increases, N / m^* rises. This implies a rise in the concentration of charge carriers is linked to an increase of thickness. One possible explanation for this is the increased concentration of Se atom lone-pair electrons with increasing film thickness [80].

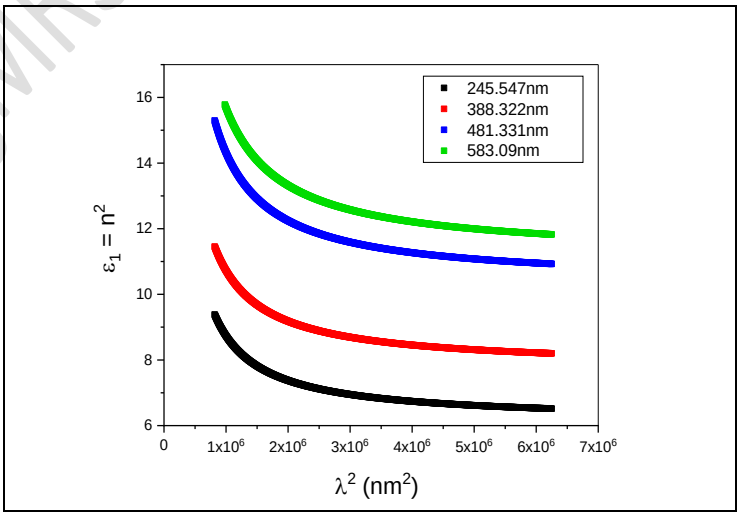

Fig.(1). plots of ε_1 against λ^2 for $Se_{49.94}Ge_{31.38}Ga_{7.38}Sb_{11.30}$ thin films.

Table 4 ε_L, ε_∞, ω_P and λ_o values for $Se_{49.94}Ge_{31.38}Ga_{7.38}Sb_{11.30}$ Films of different thicknesses.

Film thickness t (nm)	ε_L	ε_∞	N/m^* ($m^{-3}\,kg^{-1}$)	ω_P s^{-1}	λ_o (nm)
245.55 nm	7.5	7.50	1.23E+56	2.18 x10^{14}	5.29E-07
388.32 nm	9.5	9.50	2.45E+56	2.73 x10^{14}	5.38E-07
481.33 nm	12.8	12.80	3.68E+56	2.88 x10^{14}	5.51E-07
583.09 nm	14	13.99	4.91E+56	3.18x10^{14}	5.56E-07

The second approach, however, is dependent on dispersion which results from the linked carriers in an unfilled lattice. Applying a basic classical dispersion relation, the high **f** characteristics of the films are represented as a single oscillator with wavelength λ_o at high **f** [84]. The refraction index of the empty lattice n_o at infinite wavelength λ_o, n_o is given:

$$\frac{(n_o^2-1)}{(n^2-1)} = 1 - (\lambda_o/\lambda)^2 \qquad (20)$$

where λ_o and n_o were determined from the relation between $(n^2-1)^{-1}$ and λ^{-2} Fig.(14). While λ_o was calculated from the slopes, values of n_o^2 were acquired by extending lines to the y-axis.; values of ε_∞; ($\varepsilon_\infty = n_o^2$) and λ_o are shown in Table 4.

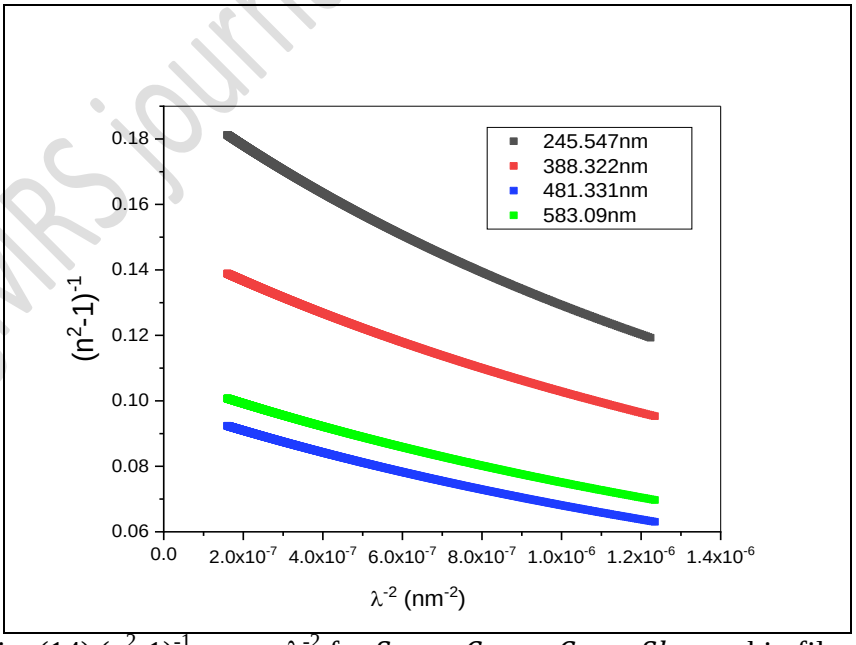

Fig. (14) $(n^2-1)^{-1}$ versus λ^{-2} for $Se_{49.94}Ge_{31.38}Ga_{7.38}Sb_{11.30}$ thin films.

The Wemple-DiDomenico (WDD Model) with Dispersion Energy Parameters.

Utilizing the single-oscillator method beneath the band gap at the visible to near-infrared region, the Wimple–DiDomenico (WDD) model [84, 85] is dependent on the n data, which is:

$$n^2 - 1 = \frac{E_o E_d}{E_o^2 - (h\nu)^2} \qquad (21)$$

where E_d (dispersion energy), which serves as a gauge for the strength of the inter-band transitions, and E_o (single oscillator energy) [74]. From the perspective of the fundamental empirical laws governing many semiconductors, these parameters are extremely valuable [86]. This is because the dispersion is important in the design of spectral dispersion devices and optical communication [74], and it influences the choice of optical material. Understanding the physical properties of materials is significantly aided by various optical parameters, such as E_d and E_o. These parameters give important details about the material's energy transitions, optical behavior, and electronic structure. E_o is energy that can excite an electron from V.B into C.B, or the average oscillator energy. It describes the material's fundamental electronic transitions. Stated differently, E_o represents the material's bandgap energy, which establishes its characteristics for absorption and transmission [87 - 89].

However, E_d stands for the average dispersion energy, or the energy needed to excite electrons in the conduction band to higher energy levels. It sheds light on the material's dispersion behavior and electron-phonon interactions. E_d has to do with the material's ability for optical dispersion and its non-linear optical characteristics. We can understand the material's energy band structure, electronic and lattice interactions, and overall optical response by interpreting these optical parameters from a physical meaning perspective. Researchers can learn more about the material's potential applications in photonics, optoelectronics, and energy harvesting by examining these parameters [78-89].

The E_o and E_d parameters for the specimen were got by plotting $(n^2\text{-}1)^{-1}$ versus $(h\upsilon)^2$. As seen fig. (15), a straight line was fitted to the lower energy data. Table 5 lists the two relations were utilized to obtain the single oscillator dispersion parameters, E_d and E_o: the intercept (E_o/E_d) and the slope $(E_o\ E_d)^{-1}$. ε_s (static high frequency dielectric constant), E_g^{WD} (wimple-DiDomenico band gap) and (static refractive index $n_s(0)$ at $h\upsilon \rightarrow 0$) , were all computed with the aid of the parameters E_d and E_o were

$$n_s(0) = \sqrt{1 + \frac{E_d}{E_o}} \quad , \qquad \varepsilon_s = (n_s(0))^2 \quad \text{and} \quad E_g^{WD} = \frac{E_o}{2} \text{ [84].}$$

values of E_o, E_d, $n_s(0)$, ε_s, and E_g^{WD} are shown in table 5 for different thicknesses.

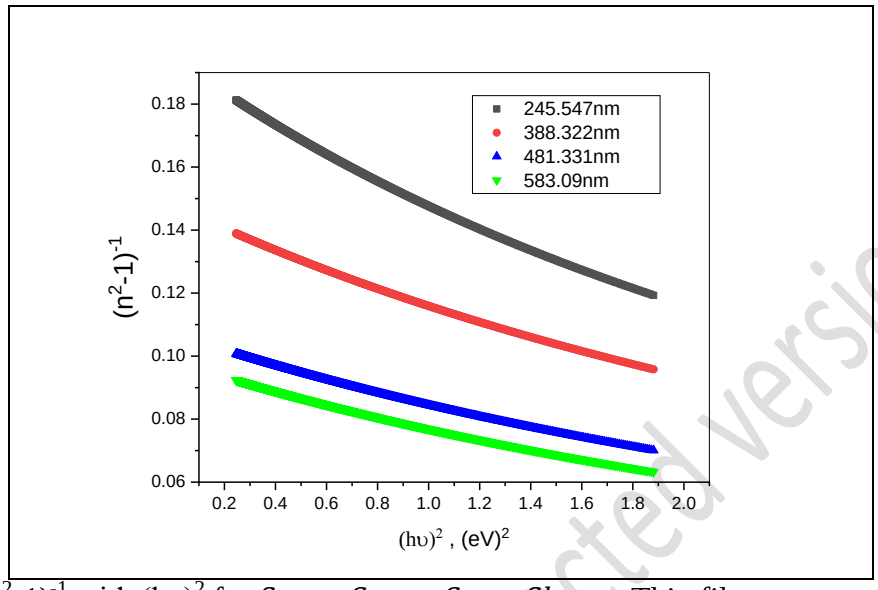

Fig.(15). $(n^2-1)^{-1}$ with $(h\upsilon)^2$ for $Se_{49.94}Ge_{31.38}Ga_{7.38}Sb_{11.30}$ Thin films.

Table 5. the Wemple–DiDomenico parameters for $Se_{49.94}Ge_{31.38}Ga_{7.38}Sb_{11.30}$ films.

Thickness t (nm)	E_d (eV)	E_o (eV)	$n_s(0)$	ε_s	E_g^{WD} (eV)
245.55 nm	13.06	2.38	2.55	6.49	1.19
388.32nm	16.40	2.35	2.83	7.99	1.17
481.33 nm	21.88	2.29	3.24	10.52	1.15
583.09 nm	22.93	2.23	3.36	11.30	1.11

Table 5 showed that while single oscillator energy E_o decreases as film thickness increases, oscillator strength (dispersion energy) E_d , ε_s and $n_s(0)$ increase.

Quantitative data regarding the material's overall band structure was estimated from the average E_o gap. More specifically, the WDD gap—the separation between centers of gravity of V.B and C.B —is what is meant to be understood by the E_o parameter. As a result, it is linked to the cohesive energy or average bond strength of the composition.

Modeling the optical constants using ANN model

The goal of this research's theoretical component is to model and forecast the optical constants for $Se_{49.94}Ge_{31.38}Ga_{7.38}Sb_{11.30}$ thin films using back propagation artificial neural network (BPANN). Simulation and prediction were done y using Matlab

programming language interface (2017a). Eight individual neural networks (ANN1-ANN8) are separately trained based on experimental data of T, refractive index, R, K, logα, ε, (n^2-1) and $(n^2-1)^2$ respectively. Three subsets of the data are used: training set 70%, test set 15% and validation set 15%. The ANN (1-8) models are perfectly trained using the input parameters table 6. Table 6 introduces the number of hidden tiers, neurons, inputs, number of training (epochs), MSE, R and finally output for eight individual networks. There was an input tier, hidden tier and output tier as shown in Fig. (16). The input tier consists of 2 neurons and output tier consists of one neuron.

The neurons number of hidden tier was fixed by trial and error method. Fig. (16) shows the network for the first ANN. Levenberg-Marqudt (LM) algorithm is the one being employed. The trainlm function is used for the training procedure in accordance with this algorithm. Trainlm is a function for training networks that relies on updating weights and biases. Tansig is a good activation function to utilize for hidden layers, and purelin is a good choice for the output layer. Tansig is the activation function that exemplifies optimal performance. The best MSE value is what the ANN aims to achieve about (10^{-5}) and regression coefficient about (1) according to Eq. (7) and (8) respectively. As seen in Fig. 17 (a-h), the network's MSE value decreased from a large number to a lesser value. Regression coefficient for the first network (ANN1) is presented in Fig. (18). The appendix contains a thorough explanation of the training algorithm. The ANN modeling results are presented in Figs. 19(a-h). Solid line curves are used to illustrate the simulated ANN results. Symbols are used to represent experimental data. Additionally, dashed lines are used to depict the expected ANN results. Figs. 19 (a-h) introduce the ANN trained, validation, testing and prediction results for T, refractive index, R, K, logα, ε, (n^2-1) and $(n^2-1)^2$respectively for the studied films of thicknesses 245.55, 338.32, 481.33 and 583.09 nm. From Figs. 19(a-h), it is seen that the experimental data symbols and the simulation ANN curves nearly coincided, indicating very good simulation results. According to this excellent agreement, we have used ANN to predict $Se_{49.94}Ge_{31.38}Ga_{7.38}Sb_{11.30}$ at thickness 100 and 430 nm especially in the areas where no experimental data are available to compare with.

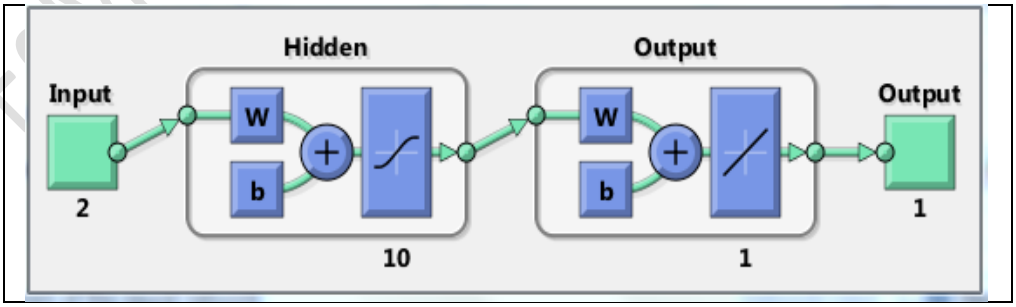

Fig.(16). (Color online) An illustration of the fundamental formal neuron network for optical constant T of $Se_{49.94}Ge_{31.38}Ga_{7.38}Sb_{11.30}$ thin film.

Table 6. ANN parameters that are employed in the estimation the of optical constants for $Se_{49.94}Ge_{31.38}Ga_{7.38}Sb_{11.30}$ thin film.

The Trained ANN	HLs	ANs	Inputs	epochs	MSE Training 70%	MSE Validation 15%	MSE testing 15%	R training	R Validation	R Testing	Out-puts
Net. 1	1	10,1	2 (λ, t)	181	5.484×10^{-4}	6.142×10^{-4}	6.066×10^{-4}	0.997	0.997	0.997	T
Net. 2	1	10,1	2(λ, t)	112	3.032×10^{-3}	3.652×10^{-3}	3.562×10^{-3}	0.991	0.991	0.989	R
Net. 3	1	4,1	2 (λ, t)	183	2.437×10^{-4}	2.674×10^{-4}	2.892×10^{-4}	0.999	0.999	0.999	n
Net. 4	1	10,1	2(λ, t)	209	5.284×10^{-6}	5.708×10^{-6}	2.673×10^{-6}	0.999	0.999	0.999	K
Net. 5	1	10,1	2 ($h\nu$, t)	810	3.542×10^{-6}	3.281×10^{-6}	4.030×10^{-6}	0.999	0.999	0.999	logα
Net. 6	1	10,1	2 (λ^2, t)	1000	5.651×10^{-7}	5.785×10^{-8}	8.227×10^{-8}	0.999	0.999	0.999	ε_1
Net. 7	1	8,1	2 (λ^{-2}, t)	84	2.488×10^{-9}	2.394×10^{-9}	2.1126×10^{-9}	0.999	0.999	0.999	$(n^2-1)^{-1}$
Net. 8	1	6,1	2($(h\nu)^2, t$)	83	5.582×10^{-9}	6.304×10^{-9}	5.524×10^{-9}	0.999	0.999	0.999	$(n^2-1)^{-1}$

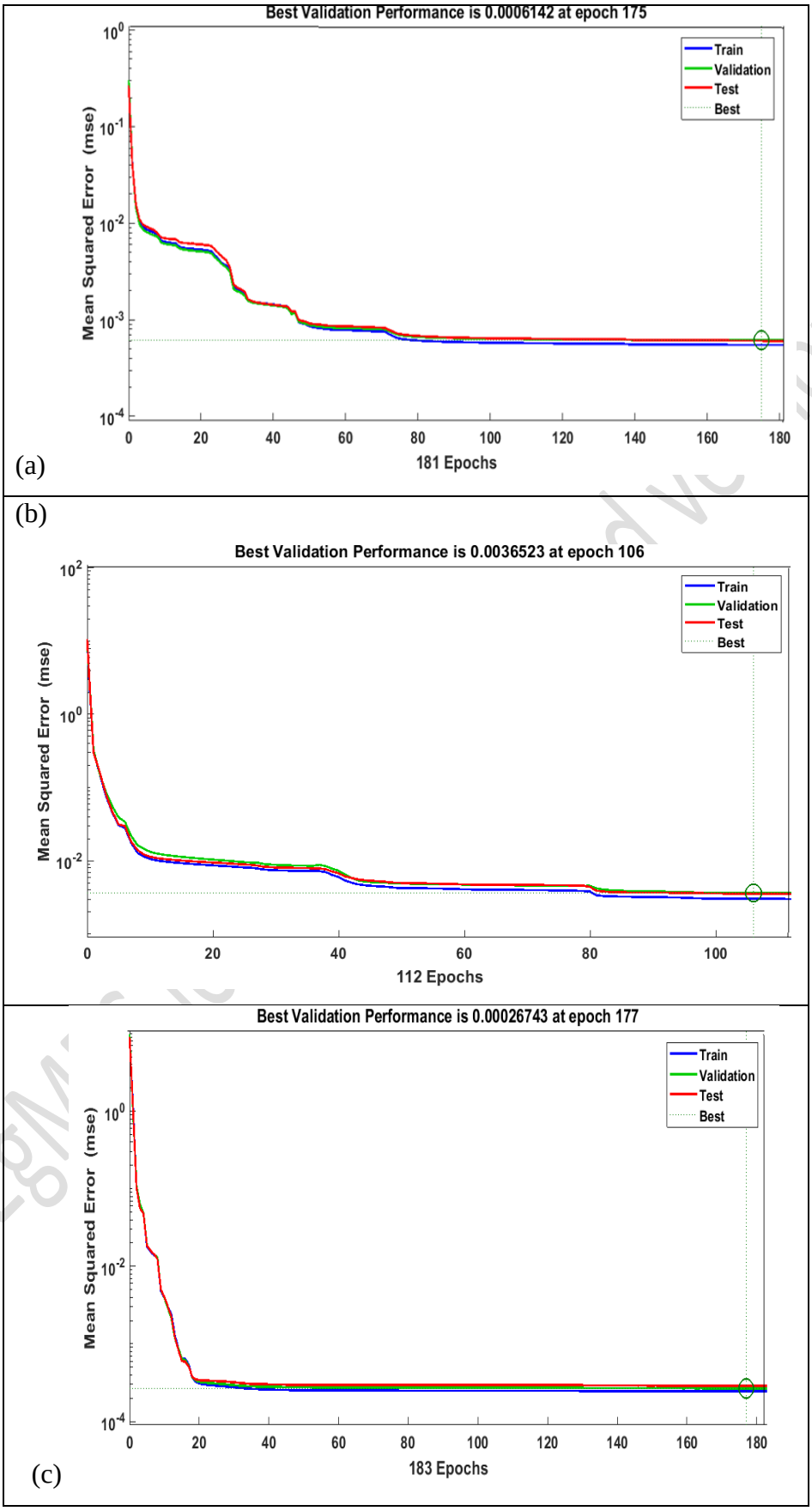
Best Validation Performance is 0.0006142 at epoch 175
Train
Validation
Test
Best
Mean Squared Error (mse)
181 Epochs
(a)
(b)
Best Validation Performance is 0.0036523 at epoch 106
Train
Validation
Test
Best
Mean Squared Error (mse)
112 Epochs
Best Validation Performance is 0.00026743 at epoch 177
Train
Validation
Test
Best
Mean Squared Error (mse)
183 Epochs
(c)

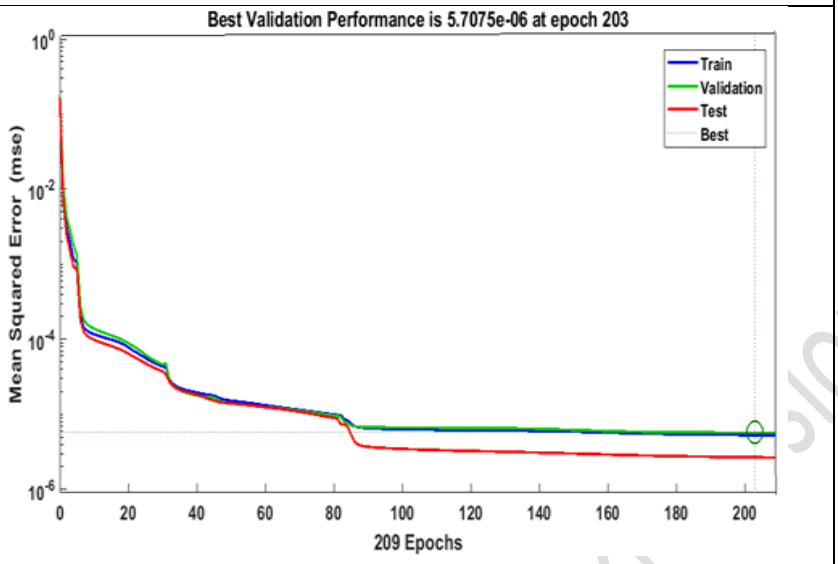
Best Validation Performance is 5.7075e-06 at epoch 203
Train
Validation
Test
Best
Mean Squared Error (mse)
209 Epochs

(d)

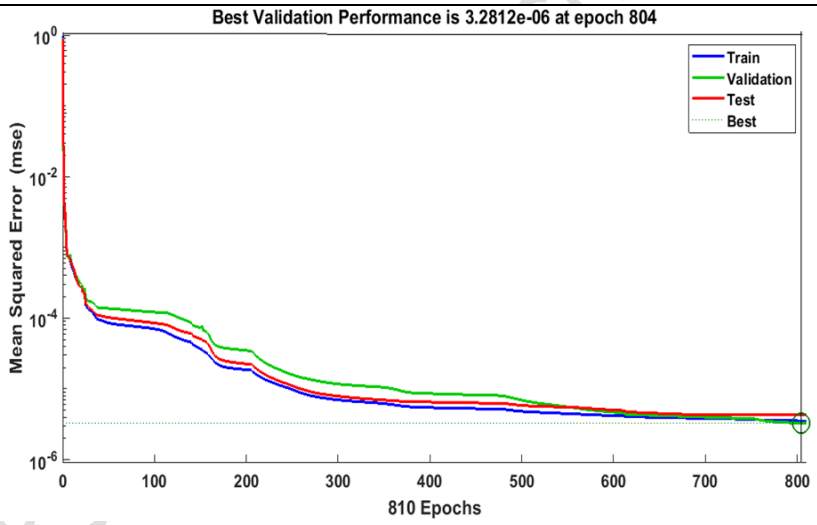
Best Validation Performance is 3.2812e-06 at epoch 804
Train
Validation
Test
Best
Mean Squared Error (mse)
810 Epochs

(e)

(f)

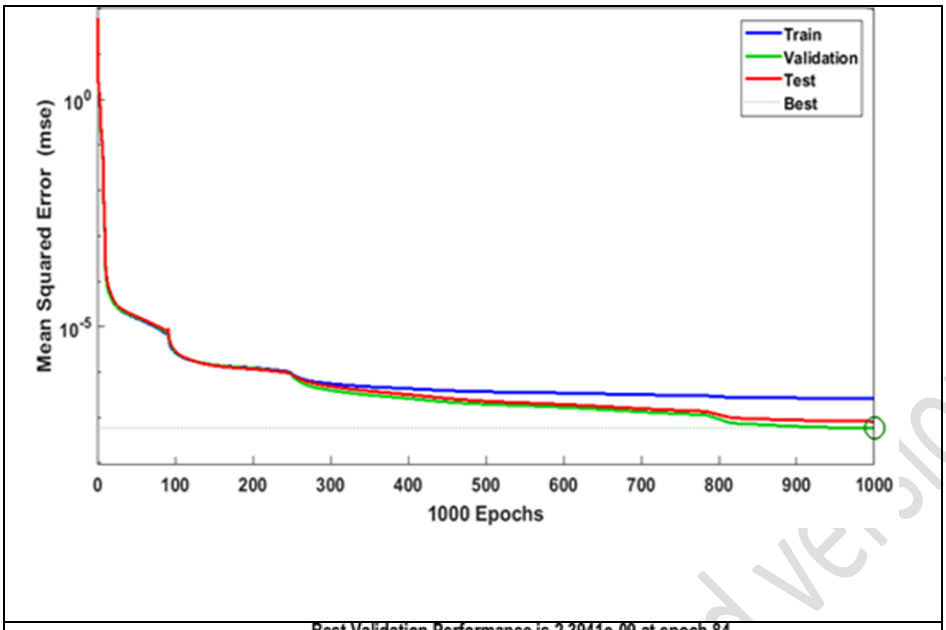
Train
Validation
Test
Best
Mean Squared Error (mse)
1000 Epochs

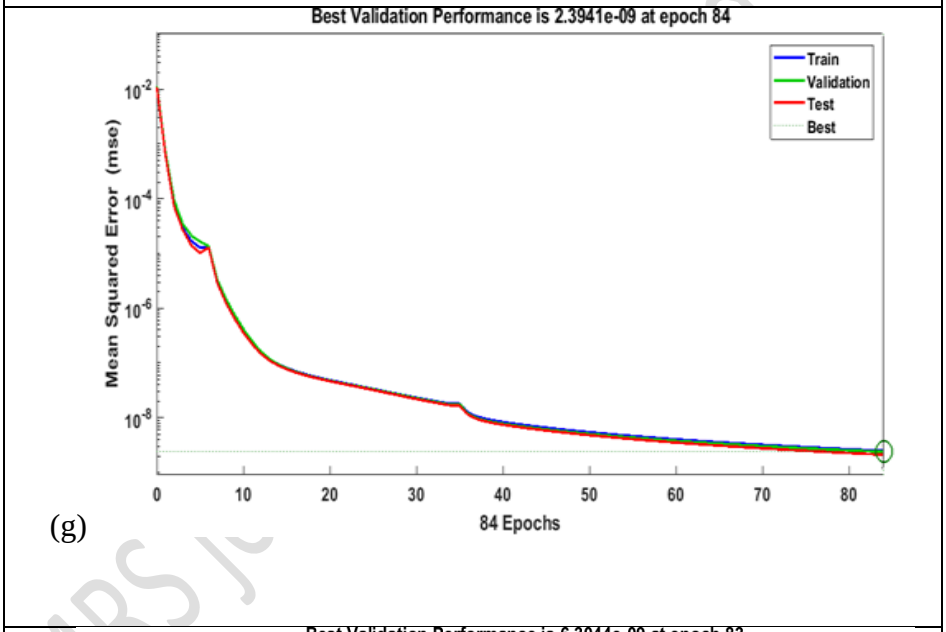
Best Validation Performance is 2.3941e-09 at epoch 84
Train
Validation
Test
Best
Mean Squared Error (mse)
84 Epochs

(g)

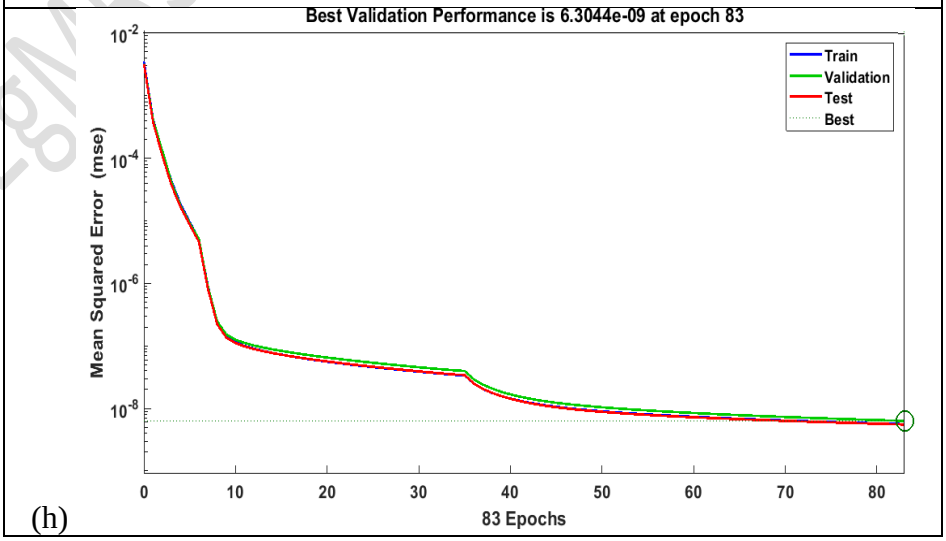
Best Validation Performance is 6.3044e-09 at epoch 83
Train
Validation
Test
Best
Mean Squared Error (mse)
83 Epochs

(h)

Fig. 17 (a-h) (color online) Top training, validation, and test sets for optical constants T, refractive index, R, K, logα, ε, (n^2-1) and $(n^2-1)^2$respectively of $Se_{49.94}Ge_{31.38}Ga_{7.38}Sb_{11.30}$ thin film.

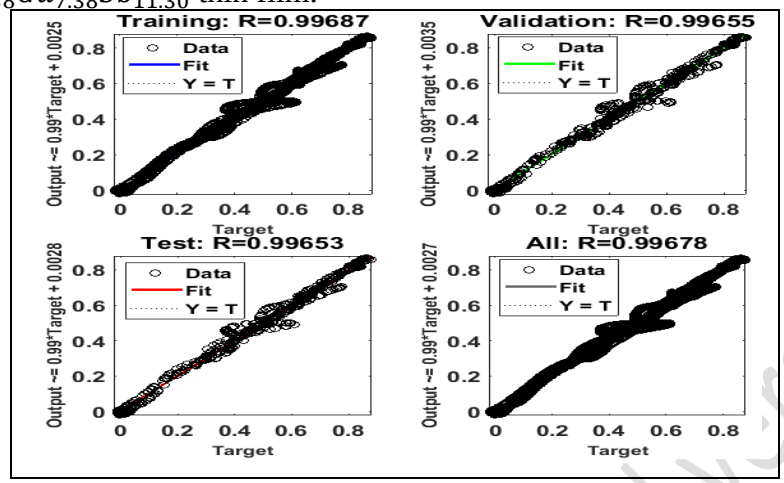

Fig. (18). Regression coefficients (R) for the test, validation, and training sets for optical constant T(ANN1) of $Se_{49.94}Ge_{31.38}Ga_{7.38}Sb_{11.30}$ thin film.

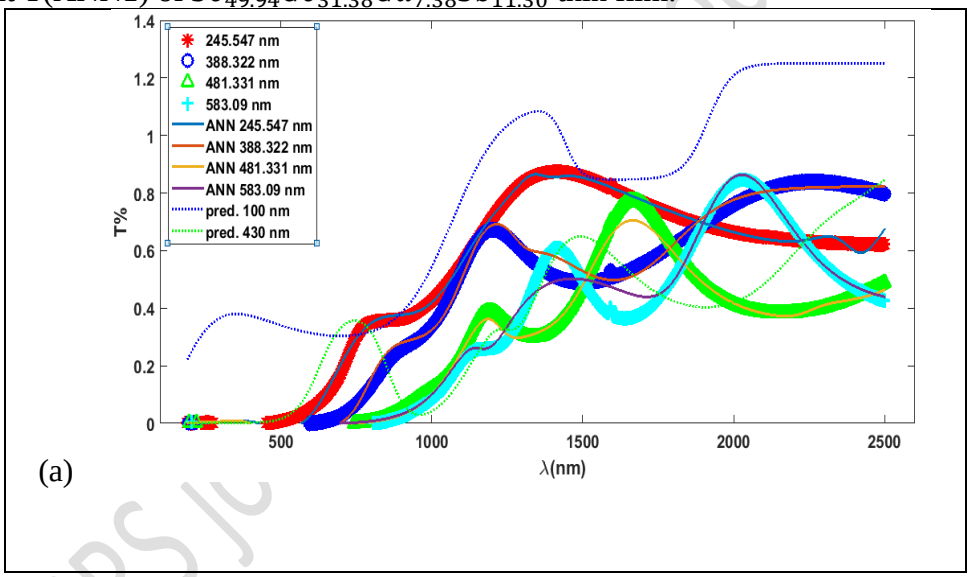

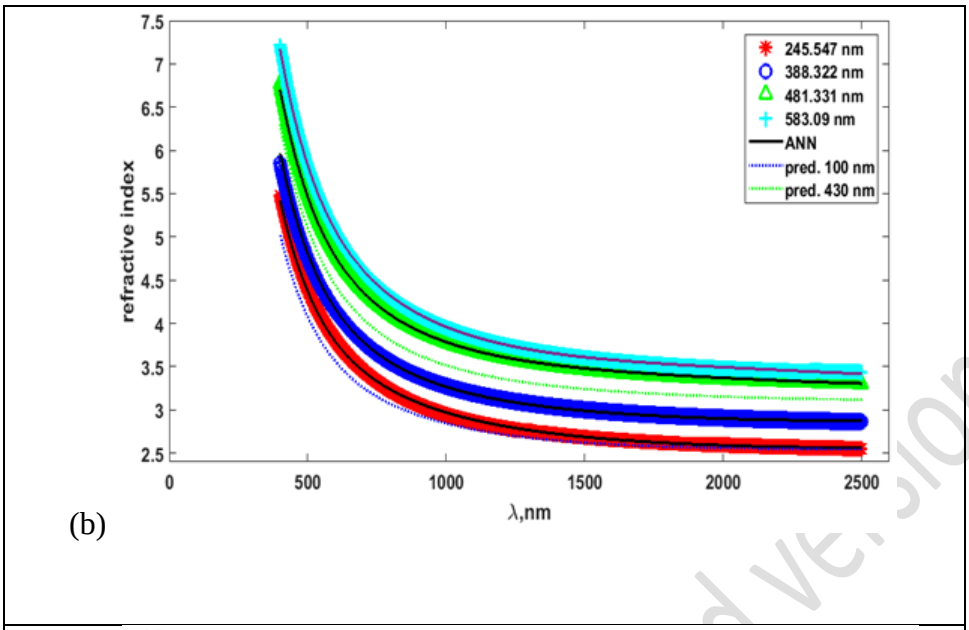
refractive index
λ,nm
245.547 nm
388.322 nm
481.331 nm
583.09 nm
ANN
pred. 100 nm
pred. 430 nm

(b)

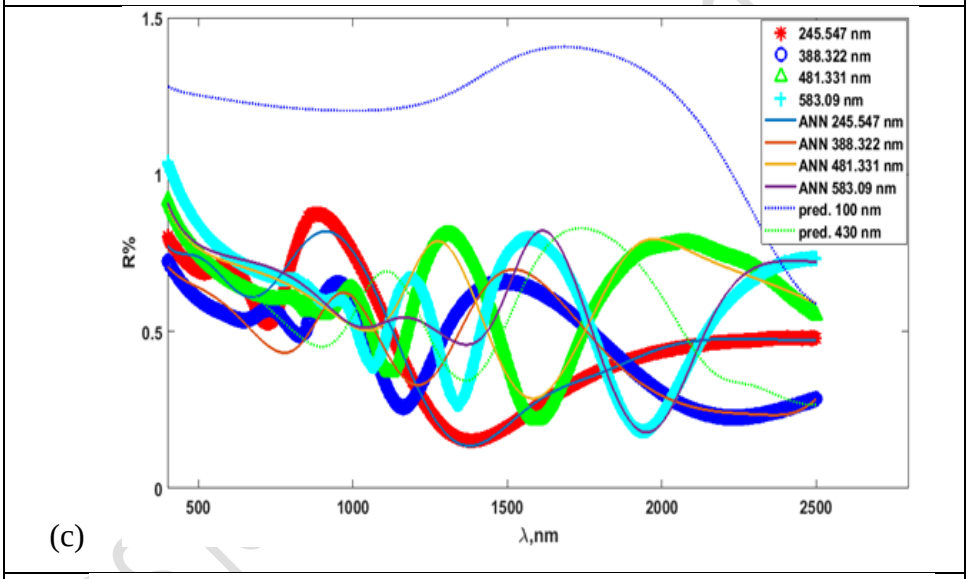
R%
λ,nm
245.547 nm
388.322 nm
481.331 nm
583.09 nm
ANN 245.547 nm
ANN 388.322 nm
ANN 481.331 nm
ANN 583.09 nm
pred. 100 nm
pred. 430 nm

(c)

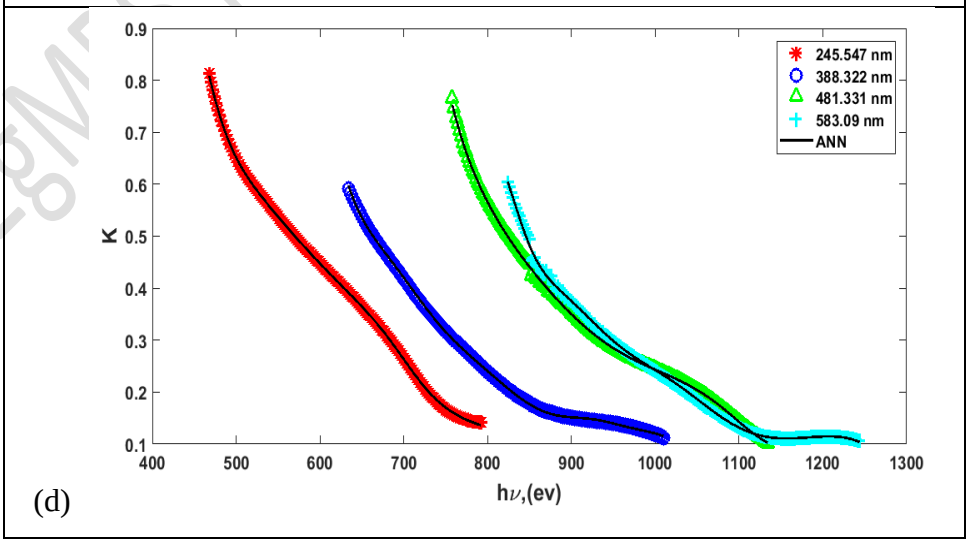
K
hν,(ev)
245.547 nm
388.322 nm
481.331 nm
583.09 nm
ANN

(d)

(e)

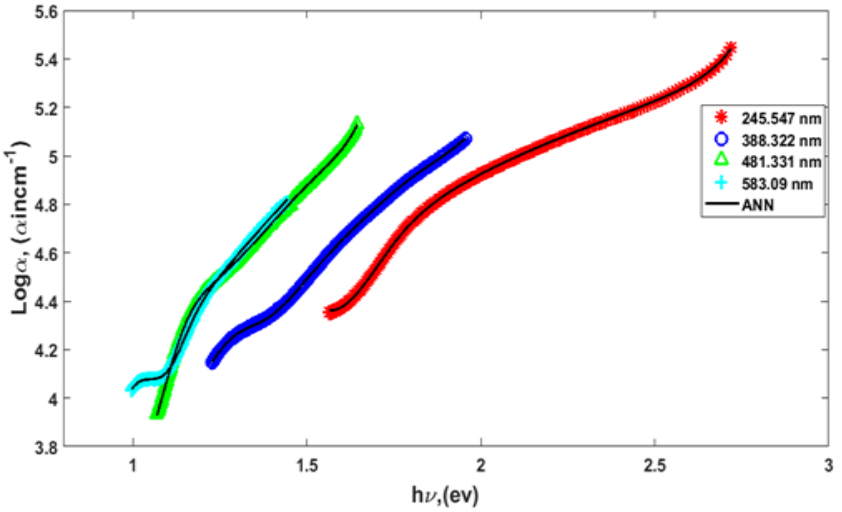
245.547 nm
388.322 nm
481.331 nm
583.09 nm
ANN
Logα, (αincm^{-1})
hν,(ev)

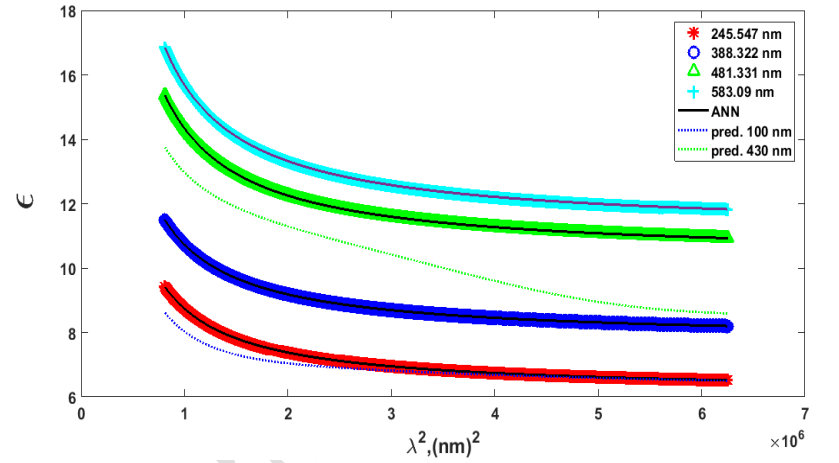
245.547 nm
388.322 nm
481.331 nm
583.09 nm
ANN
pred. 100 nm
pred. 430 nm
ϵ
λ^2,(nm)^2
×10^6

(F)

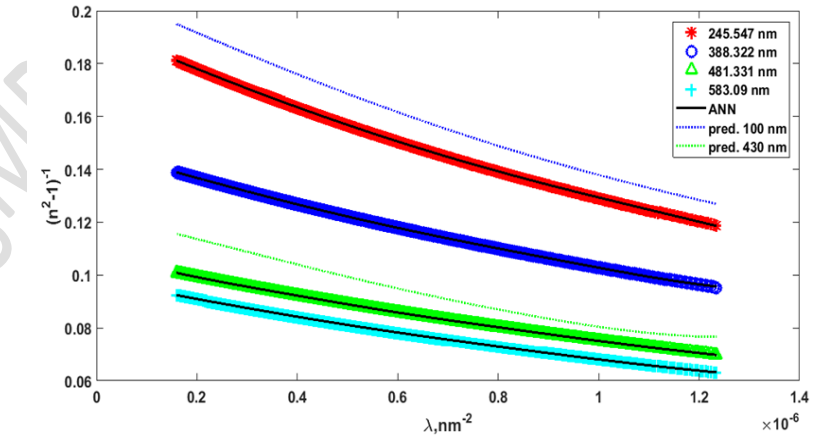
245.547 nm
388.322 nm
481.331 nm
583.09 nm
ANN
pred. 100 nm
pred. 430 nm
(n^2-1)$^{-1}$
λ,nm^{-2}
×10^{-6}

(g)

(h)

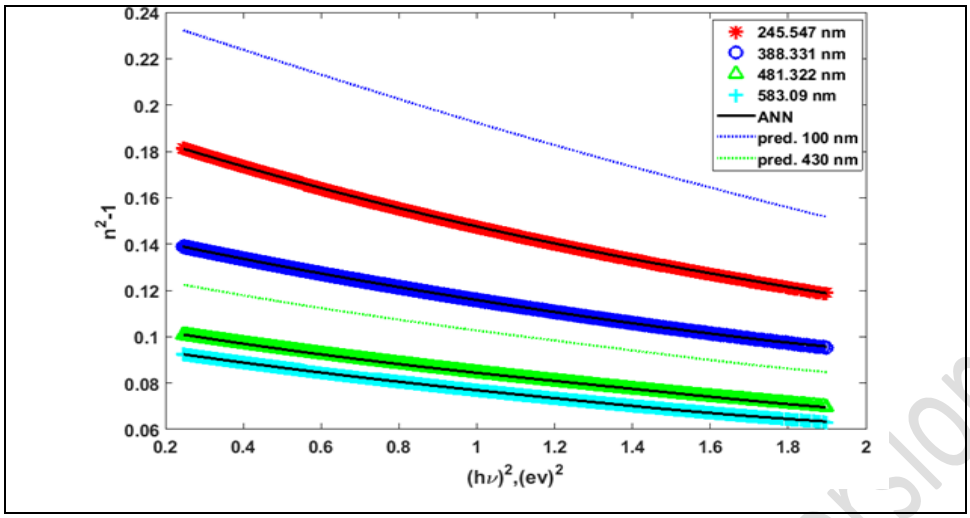

Fig. 19 (a-h). Experimental data, simulated and predicted outcomes from ANN model for optical constants T, refractive index, R, K, logα, ε, (n^2-1) and $(n^2-1)^2$ respectively of $Se_{49.94}Ge_{31.38}Ga_{7.38}Sb_{11.30}$ films at different thickness.

Conclusion:

Thin films of $Se_{49.94}Ge_{31.38}Ga_{7.38}Sb_{11.30}$ were synthesized by thermal evaporation. X-ray analysis indicated the amorphous character of the studied films. Using T(λ), the optical parameters (n, K, and α), E_g^{opt} and E_e were computed. The absorption mechanism's attribution to permitted direct and indirect transitions was verified by the optical absorption analysis. For allowed direct transition, the calculated energy gap of $Se_{49.94}Ge_{31.38}Ga_{7.38}Sb_{11.30}$ thin films changed from 1.68 eV to 1.38 eV and for allowed indirect transitions, drop from 1.28 eV to 1.05 eV as film thickness increases. The effect of increasing film thickness on the optical energy gap may be connected to a rise in structural defects that cause the film band gaps to shrink. Furthermore, the formed localized states cause the forbidden bandgap to contract, the tail to broaden, and as a result, the bandgap width to decrease. The dispersion parameters (E_d, E_o, ε_L , and N/m*) were determined, when film thickness increases, E_d and ε_s both rise. However, E_o falls. According to the previous results we may conclude that these materials are suitable for optical data storage due to their high absorption coefficient and other relevant parameters.

ANN is used to understand the effect of variation thicknesses on the optical constants of $Se_{49.94}Ge_{31.38}Ga_{7.38}Sb_{11.30}$thin films. The experimental data are employed as inputs in ANN model. ANN networks configurations which produce the minimum error are obtained.

The ANN simulated results of the optical characteristics of$Se_{49.94}Ge_{31.38}Ga_{7.38}Sb_{11.30}$ thin films are obtained and compared with the experimental data providing a successful agreement. A mathematical equation that describes the optical behavior and predictions for values that are absent from the experimental data are obtained for the under study thin

films. It is clear from the research results that ANN model gives high precision and great performance for simulating and predicting optical constants and related parameters. That introduces ANN model as an effective prediction tool that could be applied in a widely used modeling different areas in physics.

Declaration of Conflicting Interests

The author(s) declared no potential conflicts of interest concerning the research, authorship, and/or publication of this article.

Appendix A:

The formula that explains optical constants for $Se_{49.94}Ge_{31.38}Ga_{7.38}Sb_{11.30}$ filmis given by:

Optical constants = purelin [net. LW{2,1} tansig (net. IW{1,1}R+net.b{1))+net.b{2}]

where,

R is the information (inputs)

net.IW{1,1} and net.L W{1,1} are linked weights between the input layer, hidden layer and output layer respectively.

net.b{1) and net.b{2) are the bias of the hidden and output layer.

Appendix B:

Weight and bias for ANN1(T) was given as follows:

$$IW = \begin{pmatrix} 5.026312142703186 & -2.7946066983011506 \\ 17.488279344791501 & 10.763888675397096 \\ -5.7569407022742203 & 8.2948837725374247 \\ 5.930366468209046 & -3.2260212881636492 \\ 16.463213176821458 & 20.023178975090946 \\ -21.552085639789055 & -1.8372033485570476 \\ -6.7371445295025829 & 0.20644746734782052 \\ 8.245611821842358 & 21.441626869663732 \\ 14.306180015476027 & 8.135726543601276 \\ 1.5003852579156922 & 6.1629433006427554 \end{pmatrix}$$

$$LW = (\ -6.92588\ \ -0.53363\ \ 0.0685\ \ 6.67499\ \ -0.45753\ \ 0.3080\ \ -0.95068\ \ 0.79897\ \ 0.45139\ \ -0.820358)$$

$$b1 = \begin{pmatrix} 0.19100094176252172 \\ -18.030968928858556 \\ 3.4817596404077018 \\ 0.244053924792974 \\ 5.1522940197123157 \\ -1.6161918185317976 \\ -1.24190774581954 \\ 13.633567285723814 \\ 8.1079689516680169 \\ 6.0126447699170074 \end{pmatrix}$$

$$b2 = (0.047399331679381193)$$

Weight and bias for ANN2 (R) was given as follows:

$$IW = \begin{pmatrix} 5.6595903215822307 & -2.6948299452991353 \\ -7.2459404567633978 & -7.8680945057089655 \\ 6.7542751131252885 & 7.3497818965914741 \\ 3.8375518569391573 & -5.9219774009749404 \\ -6.0730180566976912 & 3.3892358838289232 \\ -3.2707929166395164 & 1.8166898356838366 \\ 4.0784858890970632 & 4.8288631803448547 \\ -8.7798269512988529 & 4.1546015274194712 \\ 8.0845882154688287 & -0.080976895889068048 \\ 3.3585985938337841 & 4.0532401317231175 \end{pmatrix}$$

$$LW = (\quad 0.0712 \quad -1.40346 \quad -1.4482 \quad -0.176086 \quad -0.456808 \quad 0.7857 \quad 1.295987 \quad -0.360 \quad -12.2046 \quad -1.563515)$$

$$b1 = \begin{pmatrix} -5.4007826526212188 \\ 6.2138852269935212 \\ -5.7773582259022547 \\ -2.0890502845735814 \\ 0.38386107080152243 \\ -0.6017771723430867 \\ 4.6048055342167595 \\ -2.8001831907321755 \\ 9.480040128798187 \\ 4.0700492058828548 \end{pmatrix}$$

$$b2 = (11.671701272757657)$$

Weight and bias for ANN3 (n) was given as follows:

$$IW = \begin{pmatrix} -0.24740975834456816 & -2.5669792681350909 \\ 1.185891064949057 & -0.76763551626791426 \\ -1.4595952409162174 & 0.11204024846113106 \\ -4.6499346746791934 & 0.052854412452844612 \end{pmatrix}$$

$$LW = (-0.16196092497162504 \quad -0.049249422394115332 \quad 3.5128553734682884 \quad 4.0947092957616338)$$

$$b1 = \begin{pmatrix} 0.063287566207915952 \\ -0.46236756875840279 \\ -2.5297465940771793 \\ -5.9133966791859551 \end{pmatrix}$$

$$b2 = (6.8120195104776471)$$

Weight and bias for ANN4 (K) was given as follows:

$$IW = \begin{pmatrix} 4.3896383539068262 & 5.832668629134643 \\ -7.5489816727947758 & 5.5706000317767845 \\ 4.0467301414368855 & 0.22469699169121549 \\ 1.8638431392092891 & 1.8899990174356833 \\ -2.4602945365798203 & -3.6908096772775458 \\ -3.7449151663413804 & -3.0802501121380703 \\ 2.3201027957293228 & 5.2233489950221479 \\ 4.2984257323322455 & 5.7563901911974238 \\ 2.9141920372622847 & 2.8139540625559323 \\ -10.989359695921568 & 5.3290130195659264 \end{pmatrix}$$

$$LW = (\quad -1.4431 \quad 0.23488 \quad -0.8803 \quad 3.12697 \quad 1.301089 \quad 2.8048 \quad 4.9401729 \quad -1.77218 \quad -0.664 \quad 0.6729)$$

$$b1 = \begin{pmatrix} -6.4763636226663568 \\ 2.6382627613949414 \\ -2.2789385391004626 \\ -2.0282812886774586 \\ 1.8179291722244832 \\ -0.74322999033205472 \\ 1.155403098013374 \\ 2.502282358091394 \\ 5.0771276317945944 \\ -6.0779392234784755 \end{pmatrix}$$

$$b2 = (0.50154609361192515)$$

Weight and bias for ANN5 (logα) was given as follows:

$$IW = \begin{pmatrix} -3.8549749689461121 & -0.4586010967773233 \\ 1.5420219324385422 & 4.7279489255231679 \\ -13.247357205429715 & -14.369588602250962 \\ -11.397190300935019 & 3.1104557688649974 \\ 1.4502103577098127 & 3.9460019067152547 \\ -0.43545575413126525 & 0.084194915913652801 \\ 11.661411317311554 & 14.864063838008768 \\ -6.6182215860029272 & -2.2108301709394627 \\ 6.9374598965960397 & 2.1957526229563826 \\ 9.8300097564784981 & -12.533883574410766 \end{pmatrix}$$

$$LW = (\quad -4.465 \quad -2.076 \quad -0.278 \quad 0.1118 \quad 2.295 \quad -8.9815 \quad 0.08086 \quad -4.49279 \quad -4.414 \quad 0.1359)$$

$$b1 = \begin{pmatrix} 5.4078105858890906 \\ -1.2502582374392257 \\ 3.2294863730536303 \\ 0.31087791698219813 \\ -0.85607277725457243 \\ -1.2804670737220225 \\ 2.51760579031607 \\ -4.4342997736980525 \\ 4.6135794641701171 \\ 13.416684494499078 \end{pmatrix}$$

$$b2 = (-2.7645751262210361)$$

Weight and bias for ANN6 (ε) was given as follows:

$$IW = \begin{pmatrix} 1.8840326812712029 & 3.3941520969945524 \\ 2.3223393892394215 & 9.2935113089359831 \\ -1.6521336607947932 & 6.8034384190406403 \\ -0.51445016005449906 & 0.044842397578894196 \\ -1.6864996569021551 & 2.204458391796515 \\ -3.3549883881492697 & -0.049423148790747828 \\ 1.3712325794818052 & -7.9917631951326351 \\ -8.3156097667915407 & 0.21487258328646913 \\ -2.1836009297012642 & 5.2106774282381902 \\ 2.080425879601342 & -2.2398942639513115 \end{pmatrix}$$

$$LW = (\quad 0.077 \quad 0.0250 \quad 0.16177 \quad 0.24425 \quad 0.105009 \quad 3.7383 \quad -0.243137 \quad 0.7816 \quad -4.496 \quad -6.140475)$$

$$b1 = \begin{pmatrix} -3.9794359911316595 \\ -2.9054970995104288 \\ 5.1139267175789733 \\ -0.76577514842573546 \\ -1.7171098036912602 \\ -5.1201923143932779 \\ 0.59226548020531944 \\ -10.141071165881792 \\ -7.7366900162693648 \\ 4.774204368463459 \end{pmatrix}$$

$$b2 = (5.988130034582797)$$

Weight and bias for ANN7 $(n^2-1)^{-1}$ was given as follows:

$$IW = \begin{pmatrix} 2.6396372713269249 & 2.6345102489220658 \\ 1.4357860404252805 & 3.7208715316301828 \\ -1.860319316161293 & 6.8034384190406403 \\ 2.0248640076784503 & 3.2961518612137719 \\ -0.26114876722025648 & 3.728194395062852 \\ -0.36346949383060345 & -0.13412258924632056 \\ -1.6449409045757133 & 2.4433743383051025 \\ 0.46887580716141014 & -4.0145808382027948 \end{pmatrix}$$

$$LW = (\quad -0.0066 \quad 0.14543 \quad 0.08195968 \quad 0.0088647 \quad -0.4397 \quad 2.132358 \quad -0.1352 \quad 0.0559)$$

$$b1 = \begin{pmatrix} -4.1313979257571454 \\ -1.9577054959839191 \\ 1.246892693987534 \\ -1.3777602223503234 \\ 0.41101450928540612 \\ -0.80314486119681061 \\ -2.4674198736419748 \\ 3.8274447992531848 \end{pmatrix}$$

$$b2 = (1.0669779668686936)$$

Weight and bias for ANN8 $(n^2-1)^{-1}$was given as follows:

$$IW = \begin{pmatrix} 2.7086730224712352 & -1.640768504239478 \\ 2.8263727319937724 & 0.69712570786451777 \\ -1.7533755211013491 & 2.4935035758743505 \\ 0.2843014873369677 & 0.40030982782098351 \\ -0.006716125240925477 4 & -3.18552100189837 \\ -0.47281137379548388 & 3.3954120319551691 \end{pmatrix}$$

$$LW = (\quad 0.00488 \quad -0.0121138 \quad 0.0221297 \quad -2.670819 \quad 0.2337879 \quad 0.183529)$$

$$b1 = \begin{pmatrix} -3.4173200690356311 \\ 1.8712976643397838 \\ 0.61133091325064892 \\ 1.0431745097372542 \\ 0.56781162018158049 \\ -3.7127945580916997 \end{pmatrix}$$

$$b2 = (1.8621335287456147)$$

References:

[1] J.G.Hernandez, E.L.Cruz, M.. Limon, B.B.Strand, S.R. Chao, Ovshinsky, "The Raman spectra of the as-deposited" Solid State Commun. Vol.95 (1995) 593.

Doi.org/10.1016/0038-1098(95)00335-5

[2] A. M. Ismail, E. G. El-Metwally, "Insight on the optoelectronic properties of novel quaternary Ge–Se–Tl–Sb non-crystalline glassy alloy films for optical fiber sensing devices". Eur. Phys. J. Plus Vol. 139 (2024) 211.

https://doi.org/10.1140/epjp/s13360-024-05012-6

[3] M. S.El-Bana, R. Bohdan, S. S.Fouad," Optical characteristics and holographic gratings recording on As30Se70 thin films". Journal of Alloys and Compounds, vol.686 (2016) 115-121.

Doi.org/10.1016/j.jallcom.2016.05.196

[4] M.Iovu, D.Harea, I. Cojocaru, E. Colomeico., A.Prisacari, V. Ciorba, "Optical properties and photoinduced absorption in As-Se and As_2Se_3: Sn thin films". Journal of Optoelectronics and Advanced Materials, vol. 9, 10 (2007) 3138-3142.

Doi.org/288044193.films

[5] D. Lezal, "Chalcogenide glasses - Survey and progress". J. Optoelectron. Adv. Mater. Vol.5, 1 (2003) 23–34.

Doi.researchgate.net/publicatiss

[6] A. K. Varshneya, "Fundamentals of Inorganic Glasses". Elsevier. (2019)

Doi.org/10.1016/C2017-0-04281-7

[7] S.Mishra, P. Kumar Singh, R.K. Yadav, A. Umar, P. Lohia, D.K. Dwivedi, "Investigation of Glass Forming Ability, Linear and Non-Linear Optical Properties of Ge-Se-Te-Sb Thin Films". Chem. Phys. Vol.541 (2021) 111021.

Doi.org/10.1016/j.chemphys.2020.111021

[8] V.Anupama, S. Thomas, "Correlation between Physical, Thermal and Optical Properties of Ge-Se-Sb Chalcogenide Glasses". AIP Conf. Proc. Vol.1849 (2017) 4984167.

Doi.org/10.1063/1.4984167

[9] J.A.Savage," Infrared Optical Materials and their Antireflection Coatings". Adam Hilger, Bristol. Vol 17(1985) 273.

Doi.org/10.1016/0030-3992(85)90043-X

[10] S.R.Elliott, " Physics of Amorphous Materials". Longman, New York. (1990)

Doi.org/10.1002/crat.2170200922

[11] Z.Cimpl, F.Kosek, " Refractive index of As2−xSbxS3 and As2−xSbxSe3 Systems" Phys. Phys. Stat. Sol. (a) vol.93 (1986) K55.

Doi.org/10.1002/pssa.2210930164

[12] P.Priyadarshini, S. Das, R. Naik, "A Review on Metal-Doped Chalcogenide Films and Their Effect on Various Optoelectronic Properties for Different Applications". RSC Adv. Vol.12 (2022) 9599–9620.

Doi.org/10.1039/D2RA00771A

[13] X. Zhang, H. Ma, J. Adam, J. Lucas, G. Chen, D. Zhao, " Thermal and Optical Properties of the Ga-Ge-Sb-Se Glasses". Mater. Res. Bull. Vol.40 (2005) 1816–1821.

[14] H. Guo, H. Zhang, L. Liu, X. Xiao, 'G. Farrell, " Industrial, Medical and Military Applications of Fluoride and Chalcogenide Glass Fibers" Springer: Singapore (2022) 327–370.

Doi.org/10.1016/j.materresbull.2005.05.003

[15] S.Mishra, P. Lohia, D.K. Dwivedi, "Structural and Optical Properties of (Ge11.5Se67.5Te12.5)100−x Sbx ($0 \leq x \leq 30$) Chalcogenide Glasses" A Material for IR Devices. Infrared Phys. Technol. Vol.100 (2019) 109–116.

Doi.org/10.1016/j.infrared.2019.05.001

[16] R. Mondal, D. Biswas, S. Paul, A.S.Das, C. Chakrabarti, D.Roy, S. Bhattacharya, S. Kabi, "Investigation of microstructural, optical, physical properties and dielectric relaxation process of sulphur incorporated selenium–tellurium ternary glassy systems". Mater. Chem. Phys. Vol.257 (2021) 123793.

Doi.org/10.1016/j.matchemphys.2020.123793

[17] A.M.Shakra, E.G. El-Metwally, " Determination of allowed transition types and the optical parameters of Se–Ge–Ag chalcogenide films". Eur. Phys. J. B vol.91 (2018) 245.

Doi.org/10.1140/epjb/e2018-90273-7

[18] A.M.Shakra, M. Fadel, A.E. Kalila, " The effect of cadmium and zinc additives on the transition temperatures and crystallization kinetics of glassy Se98Te alloy". Indian J. Phys. Vol. 95(4) (2020) 595-606.

Doi.org/10.1007/s12648-020-01715-5

[19] A. M. Shakra,I. S. Yahia,S. S. Shenouda, "Determination of the refractive index of indigo dye thin film/flexible polyacetate substrate". Optical and Quantum Electronics vol.55 (2023) 823.

Doi.org/10.1007/s11082-023-05014-1

[20] A.S.Hassanien, L. Sharma,"Optical Properties of Quaternary A-Ge15−xSbxSe50Te35 Thermally Evaporated Thin-Films: Refractive Index Dispersion and Single Oscillator Parameters" Optik, vol.200 (2020) 163415

Doi.org/10.1016/j.ijleo.2019.163415

[21] I.Pethes, R. Chahal, V.Nazabal, C. Prestipino, S. Michalik, J. Darpentigny, P. Jóvári, " Chemical Order in Ge-Ga-Sb-Se Glasses". J. Non. Cryst. Solids vol.484 (2018) 49–56.

Doi.org/10.1016/j.jnoncrysol.2018.01.017

[22] M.A.Abdel-Rahim, M.M. Hafiz, A.Z. Mahmoud, " Effect of Sb Additive on Structural and Optical Properties of Se–Te–Sb Thin Films". Appl. Phys. A Mater. Sci. Process.vol.118 (2015) 981–988.

Doi.org/10.1007/s00339-014-8853-x

[23] C.Liu, Y. Yuan, L. Cheng, J. Su, X. Zhang, X. Li, H. Zhang," Study on Optical Properties of Sb2Se3 Thin Films and Resistive Switching Behavior in Ag/Sb2Se3 /W Heterojunctions". Results Phys. vol.13 (2019) 102228.

Doi.org/10.1016/j.rinp.2019.102228

[24] Z. G. Ivanova, V. Pamukchiva, and M. Vlcek., "On the structural phase transformations in GexSb40−xSe60 glasses". Journal of Non-Crystalline Solids, vol.580 (2001) 293-295.

Doi.org/10.1016/S0022-3093(01)00842-0

[25] S. Mahadevan and A. Giridhar, “Floppy to rigid transition and chemical ordering in Ge—Sb(As)—Se glasses ’’. Journal of Non-Crystalline Solids, vol.143 (1992) 52–58.

Doi.org/10.1016/S0022-3093(05)80552-6

[26] P. Kumar, J. Kaur, S. K. Tripathi & I. Sharma , "Effect of antimony (Sb) addition on the linear and non-linear optical properties of amorphous Ge–Te–Sb thin films". Indian J. Phys., vol.91 (2017) 1503-1511.

Doi.org/10.1007/s12648-017-1053-8

[27] N.S.Saxena, " Phase Transformation Kinetics and Related Thermodynamic and Optical Properties in Chalcogenide Glasses". J. non-Cryst. Solids, vol. 345(2004) 161–168.

Doi.org/10.1016/j.jnoncrysol.2004.08.016

[28] E.V.Karaksina, V.S. Shiryaev, A.I. Filatov, A.D. Plekhovich, "Effect of Ge-Rich Ga-Ge-Sb-Se Glass Composition on the Optical and Thermal Properties". Opt. Mater. Vol.104 (2020) 109943.

Doi.org/10.1016/j.optmat.2020.109943

[29] M.I. Alonso, K. Wakita, J. Pascual, N. Yamamoto, "Optical functions and electronic structure of CuInSe2, CuGaSe2, CuInS2, and CuGaS2". Phys. Rev. B.vol 63 (2001) 75203.

Doi.org/10.1103/PhysRevB.63.075203

[30] Xiaoshu Jiang, W.R.L. Lambrecht, "Electronic band structure of ordered vacancy defect chalcopyrite compounds with formula II−III2−VI4." Phys. Rev. B.vol 69 (2004), 035201.

Doi.org/10.1103/PhysRevB.69.035201

[31] R. Marquez, C. Rincon, "On the Dielectric Constants of AIBIIIC Chalcopyrite Semiconductor Compounds "Phys. Status Solidi. Vol 191 (1995) 115.
Doi.org/10.1002/pssb.2221910112

[32] Zhang, X.; Ma, H.; Adam, J.L.; Lucas, J.; Chen, G.; Zhao, D., "Thermal and Optical Properties of the Ga-Ge-Sb-Se Glasses". Mater.Res. Bull. vol 40, (2005)1816–1821. [CrossRef]
Doi.org/10.1016/j.materresbull.2005.05.003

[33] Liu, K.; Kang, Y.; Tao, H.; Zhang, X.; Xu, Y. "Effect of Se on Structure and Electrical Properties of Ge-As-Te Glass". Materials. Vol 15, (2022)1797. [CrossRef]
Doi.org/10.3390/ma15051797

[34] Guo, H.; Zhang, H.; Liu, L.; Xiao, X.; Farrell, G. "Industrial, Medical and Military Applications of Fluoride and Chalcogenide Glass Fibers." Springer: Singapore, (2022); pp. 327–370. [CrossRef]

Doi.org/10.1007/978-981-16-7941-4_9

[35] Priya Kush, and Sasanka Deka, "Multifunctional Copper-Based Quaternary Chalcogenide Semiconductors Toward State-of-the-Art Energy Applications." ChemNanoMat . vol 5 (2019) 373–402 Sasanka Deka.

Doi.org/10.1002/cnma.201800321

[36] Muneer Ahmad, J. Kumar, R. Thangaraj, "Electrical and optical properties of $Sn_{10}Sb20\_xBi_xSe_{70}$ glassy films." Journal of Non-Crystalline Solids. vol 355(2009) 2345–2348.

Doi.org/10.1016/j.jnoncrysol.2009.08.015

[37] Vandita Rao, N. Chandel, N. Mehta & D. K. Dwivedi, " Effect of antimony on glass transition and thermal stability of Se78−xTe18Sn2Sbx (x = 0, 2, 4 and 6 at.%) multicomponent glassy alloys". Journal of Thermal Analysis and Calorimetry. Vol (2018) 134 915-922 .

Doi.org/10.1007/s10973-018-7309-5

[38] Wencong Shi, Tribhuwan Pandey, Lucas Lindsay, and Lilia M. Woods., "Vibrational properties and thermal transport in quaternary chalcogenides: The case of Te-based compositions". Physical review materials. vol 5 (2021), 045401.

Doi.org/10.1103/PhysRevMaterials.5.045401

[39] B.A. Mansour, S.A. Gada, Hoda Mohamed Eissa, "effect of γ-irradiation on the optical and electrical properties of PbxGe42−xSe48Te10". Journal of Non-Crystalline Solids.vol 412 (2015) 53-57.

Doi.org/10.1016/j.jnoncrysol.2015.01.006

[40] Borah, D.J.; Mostako, A.T.T., "Investigation on Dispersion Parameters of Molybdenum Oxide Thin Films via Wemple-DiDomenico (WDD) Single Oscillator Model". Appl. Phys. A. vol 126 (2020) 818.

Doi.org/10.1007/s00339-020-03996-3

[41] Singh, P.; Kumar, R., "Investigation of Refractive Index Dispersion Parameters of Er Doped ZnO Thin Films by WDD Model". Optik.vol 246 (2021) 167829.

Doi.org/10.1016/j.ijleo.2021.167829

[42] Hassanien, A.S.; Sharma, I.; Akl, A.A., "Physical and Optical Properties of A-Ge-Sb-Se-Te Bulk and Film Samples: Refractive Index and Its Association with Electronic Polarizability of Thermally Evaporated a-Ge15-XSbxSe50Te35 Thin-Films". J. Non. Cryst. Solids.vol 531(2020), 119853.

Doi.org/10.1016/j.jnoncrysol.2019.119853

[43] Abdel-Wahab, F.; Ali Karar, N. N.; El Shaikh, H.A.; Salem, R.M., "Effect of Sb on the Optical Properties of the Ge-Se Chalcogenide Thin Films". Phys. B Condens. Matter. vol 422 (2013) 40–46.
Doi.org/10.1016/j.physb.2013.04.010

[44] J. Tauc, R. Grigorovici, A. Vancu., "Optical properties and electronic structure of amorphous germanium". Physica Status Solidi (b). vol 15 (1966) 627-637.
Doi.org/10.1002/pssb.19660150224

[45] S.S. Fouad, M.S. El-Bana, P. Sharma, V. Sharma., "Analysis of chemical ordering and fragility for Ge–Se–In glasses". Applied Physics A. vol 120 (2015) 137-143.
Doi.org/10.1007/s00339-015-9180-6

[46] A.A. Attia, M.M. El-Nahass, M.Y. El-Bakry, D.M. Habashy, "Neural networks modeling for refractive indices of semiconductors". Optics Communications. vol 287 (2013) 140-144.
Doi.org/10.1016/j.optcom.2012.09.016

[47] Ch. Bourouis, A. Meddour, A.K. Moussaoui, "Determination of optical properties of Al80Mn20 quasi-crystalline alloy using neural networks." Journal of Molecular Structure: THEOCHEM. vol 777 (2006) 45-51.
Doi.org/10.1016/j.theochem.2006.08.010

[48] A. A. Attia, M. S. El-Bana, D. M. Habashy, S.S. Fouad, "Optical constants characterization of $As_{30}Se_{70-x}Sn_x$ thin films using neural networks". Journal of Applied Research and Technology. Vol 15 (2017) 423.
Doi.org/10.1016/j.jart.2017.03.009

[49] M. F. Tabet, W. A. McGahan, "Use of artificial neural networks to predict thickness and optical constants of thin films from reflectance data". Thin Solid Films. vol 370 (2000). 122-127.
Doi.org/10.1016/S0040-6090(00)00952-4

[50] L. Fan, A. Chen, T. Li, J. Chu, Y. Tang, J. Wang, M. Zhao, T. Shen, M. Zheng, F. Guan, H. Yin, L. Shi, J. Zi, "Thin-film neural networks for optical inverse problem." Light: Advanced Manufacturing. (2021).
Doi.org/10.37188/lam.2021.027

[51] S. M. Kim, S. Dildar, Haider Naqvi, M. G. Kang, H. Song, and S. Ahn, "Optical Characterization and Prediction with Neural Network Modeling of Various Stoichiometries of Perovskite Materials Using a Hype regression Method." Nanomaterials. vol 12 (2022) 932.
Doi.org/10.3390/nano12060932

[52] T. I. Haweel, M. Y. El-Bakry, K. A. El-Metwally, "Hadron–hadron interactions at high energy via Rademacher functions." Chaos, Solitons & Fractals. vol 18 (2003) 159-168.

Doi.org/10.1016/S0960-0779(02)00581-7

[53] H. A. M. Ali and D M Habashy, "The electrical impedance, AC conductivity and dielectric properties of phenol red compound investigated and modeled by an artificial neural network, Commun". Theor. Phys.vol 72 (2020) 105701.

Doi.org/10.1088/1572-9494/aba24d

[54] A.M.A. El-Barry, R. A. Mohamed. "Modeling of Photovoltaic characteristics of pyronine thin film/P-Si single". Material Research Express. Vol 6 (2019) 076419-076431.

Doi.org/10.1088/2053-1591/ab0a34

[55] R. A. Mohamed, "Modeling of electrical properties of nanofluids using artificial neural network." Physica Scripta. Vol 94 (2019) 105222-105233.

Doi.org/10.1088/1402-4896/ab1939

[56] R. A. Mohamed," Prediction of AC conductivity for organic semiconductors based on artificial neural network ANN model." Material Research Express. vol 6 (2019) 085107-085121.

Doi.org/10.1088/2053-1591/ab250a

[57] H.A.M. Ali, E.F.M. El-Zaidia, R.A. Mohamed, "Experimental investigation and modeling of electrical properties for phenol red thin film deposited on silicon using back propagation artificial neural network". Chinese Journal of Physics. vol 67 (2020) 602–614.

Doi.org/10.1016/j.cjph.2020.07.018

[58] R. A. Mohamed, "Application of artificial neural network model for prediction of thermo–physical properties of carbon nanotubes (CNTs) containing nanofluid." Journal of Nanofluids. 8 (2019) 199 – 204.

Doi.org/10.1166/JON.2019.1573

[59] Ö. Kişi, E. Uncuoglu, "Comparison of three-back-propagation training algorithms for two case studies".Indian Journal of engineering and materials sciences. Vol 12 (2005) 434-442.

[60] Ch. C. Aggarwal, "Neural Networks and Deep Learning; A textbook". (2018)

Doi.org/10.1007/978-3-319-94463-0

[61] A. F. Abd El-Rehim, D. M. Habashy, H. Y. Zahran, H. N. Soliman., "Mathematical Modelling of Vickers Hardness of Sn-9Zn-Cu Solder Alloys Using an Artificial Neural Network". Metals and Materials International. vol (2021) 274084–4096.

Doi.org/10.1007/s12540-020-00940-1

[62] D. M. Habashy, Mahmoud Y. El-Bakry, Werner Scheinast, Mahmoud Hanafy., "Entropy per Rapidity in Pb-Pb Central Collisions using Thermal and Artificial Neural Network (ANN) Models at LHC Energies". Chinese Physics C.vol 46 (2022) 073103.

Doi.org/10.1088/1674-1137/ac5f9d

[63] J. A. K. Suykens, J. P. L. Vandewalle, B. L. R. De Moor, "Artificial Neural Networks for Modelling and Control of Non-Linear Systems". (1996).

Doi.org/10.1007/978-1-4757-2493-6

[64] El-Metwally, E.G., Hegab, N.A.; Mostfa, M., **"**Linear and Non-Linear Optical Dispersion Parameters of Te81Ge15Bi4 Chalcogenide Glass Thin Films for Optoelectronic Applications". Phys. B Condens. Matter.vol 626 **(**2022) 413556.

Doi.org/10.1016/j.physb.2021.413556

[65] Swanepoel, R., "Determination of the Thickness and Optical Constants of Amorphous Silicon". J. Phys. E. vol 16 (1983) 1214.

Doi.org/10.1088/0022-3735/16/12/023

[66] Fadel, M.; Fayek, S. A.; Abou-Helal, M.O.; Ibrahim, M. M.; Shakra, A. M., "Structural and Optical Properties of SeGe and SeGeX (X = In, Sb and Bi) Amorphous Films". J. Alloys Compound. Vol 485 (2009) 604–609.

Doi.org/10.1016/j.jallcom.2009.06.057

[67] Huda Allah Abou-Elnour, M. B. S. Osman, M. Fadel and A. M. Shakra, "Investigation of the Optical Properties for Quaternary $Se_{60-X}Ge_{35}Ga_5Sb_X$ (x = 0, 5, and10)Chalcogenide Glass". Materials. vol 15(2022)6403.

Doi.org/10.3390/ma15186403

[68] A. M. Shakra, G. F. Salem, "The optical properties of Se85.26Ge12.92Cd1.81 thin films on different substrates", Optical and Quantum Electronics. vol 53 (2021) 497 Doi.org/10.1007/s11082-021-03156-8

[69] Hegab, N. A.; Farid, A. S.; Shakra, A. M.; Afifi, M. A.; Alrebati, A. M., "Compositional Dependence of the Optical Properties of Amorphous Semiconducting Glass Se80Ge20−xCdx (0 ≤ x ≤ 12 at. %) Thin Films". J. Electron. Mater.vol 45 (2016) 3332–3339. [Google Scholar]

Doi: 10.1007/s11664-016-4470-0

[70] Bhira, L.; Essaidi, H. ; Belgacem, S. ; Couturier, G.; Salardenne, J.; Barreaux, N.; Bernede, J.C., "Structural and Photoelectrical Properties of Sprayed β-In2S3 Thin Films". physica status solidi (a). Vol 181 (2000) 427-435. [Google Scholar]
Doi.org/10.1002/1521-396X(200010)181:2%3C427::AID-PSSA427%3E3.0.CO;2-P

[71] Paunovic, P.; Kulisch, W.; Popov, C.; Petkov, P., "Nanotechnological Basis for Advanced Sensors"; Springer: Berlin/Heidelberg, Germany. vol 53 (2011) 1689–1699 [CrossRef]

Doi.org/10.1007/978-94-007-0903-4

[72] Li, J.; Wu, S.-T., "Extended Cauchy Equations for the Refractive Indices of Liquid Crystals". J. Appl. Phys. vol 95 (2004) 896–901. [Google Scholar]

Doi.org/10.1063/1.1635971

[73] Urbach, F., "The Long-Wavelength Edge of Photographic Sensitivity and of the Electronic Absorption of Solids". Phys. Rev. vol 92(1953) 1324.

Doi.org/10.1103/PhysRev.92.1324

[74] Fadel, M.; Yahia, I.S.; Sakr, G.B.; Yakuphanoglu, F.; Shenouda, S.S., "Structure, Optical Spectroscopy and Dispersion Parameters of ZnGa2Se4 Thin Films at Different Annealing Temperatures". Opt. Communications. Vol 285 (2012) 3154–3161.

Doi.org/10.1016/j.optcom.2012.02.096

[75] Ilican, S.; Caglar, Y.; Caglar, M.; Yakuphanoglu, F.,"The Effects of Substrate Temperature on Refractive Index Dispersion and Optical Constants of CdZn(S0.8Se0.2)2 Alloy Thin Films". J. Alloys Compd., vol 480 (2009) 234–237.
Doi.org/10.1016/j.jallcom.2009.02.117

[76] J. Tauc, "Amorphous and Liquid Semiconductors" Springer US (1974).

Doi.org/10.1007/978-1-4615-8705-7

[77] J. Tauc, R. Grigorovici, A. Vancu, "Optical Properties and Electronic Structure of Amorphous Germanium." Phys. Status Solidi b.vol 15 (1966) 627–637 .

Doi.org/10.1002/pssb.19660150224

[78] Mott, N. F., & Davis, E. A., "Electronic processes in non-crystalline materials". Physics Today . vol 25(1972) 55.

Doi.org/10.1063/1.3071145

[79] V.B. Sandomirskii, " Quantum Size Effect in a Semimetal Film"
Sov. Phys. JETP. Vol 25(1) (1967) 101.

Doi.org/Semimetal NASA/ADS (harvard.edu)

[80] Ahmed Saeed Hassanien, Hatem R. Alamri· I. M. El Radaf, "Impact of film thickness on optical properties and optoelectrical parameters of novel CuGaGeSe4 thin films synthesized by electron beam deposition" Optical and Quantum Electronics. vol 52 (2020) 335.

Doi.org/10.1007/s11082-020-02448-9

[81] Hameed, T.A., Wassel, A.R., El Radaf, I.M., "Investigating the effect of thickness on the structural,morphological, optical and electrical properties of AgBiSe2 thin films". J. Alloys Compd.vol 805 (2019) 1–11.

Doi.org/10.1016/j.jallcom.2019.07.041

[82] Hassanien, A.S., Akl, A.A., "Influence of composition on optical and dispersion parameters of thermally evaporated non-crystalline Cd50S50−xSex thin films". J. Alloys Compd. vol 648 (2015) 280–290.

Doi.org/10.1016/j.jallcom.2015.06.231

[83] Zemel, J.N.; Jensen, J.D.; Schoolar, R.B., "Electrical and Optical Properties of Epitaxial Films of PbS, PbSe, PbTe, and SnTe". Phys. Rev.vol 140 (1965) A330.

Doi.org/10.1103/PhysRev. 140.A330

[84] Wemple, S.H.; DiDomenico, M., "Behavior of the Electronic Dielectric Constant in Covalent and Ionic Materials". Phys. Rev. B. vol 3 (1971) 1338–1351.

Doi.org/10.1103/PhysRevB.3.1338

[85] S.H. Wemple, "Refractive-Index Behavior of Amorphous Semiconductors and Glasses". Phys. Rev. B. vol 7 (1973) 3767.

Doi.org/10.1103/PhysRevB.7.3767

[86] D. J. Borah, A.T.T. Mostako, "Investigation on dispersion parameters of Molybdenum Oxide thin films via Wemple–DiDomenico (WDD) single oscillator model ."Appl. Phys. A Mater. Sci. Process. Vol 126 (2020) 1–13.

Doi.org/10.1007/s00339-020-03996-3

[87] D. P. Ghosh, M. K. Naskar, S. K. Batabyal, "Optical properties of semiconductor nanoparticles." Journal of Nanoparticle Research.vol 11, no. 3 (2009) 529-541.

Doi:10.1007/s11051-013-2121-0.

[88] S. N. Ghosh, J. M. Hui, "Optical properties of nanostructured materials". Journal of Materials Science: Materials in Electronics. vol 26, no. 6 (2015) 4083-4103.

Doi:10.1007/s10854-014-2713-9.

[89] P. Pavani, S. Adarsh, "Interband and intraband optical transitions in semiconductor nanostructures" Journal of Applied Physics. vol 125, no. 5 (2019) 055301.

Doi: 10.1063/1.5086415.